



High-energy proton induced damage in PbWO_4 calorimeter crystals

M. Huhtinen

CERN, CH-1211 Geneva, Switzerland

P. Lecomte, D. Luckey, F. Nessi-Tedaldi, F. Pauss

Swiss Federal Institute of Technology (ETH), CH-8093 Zürich, Switzerland

Abstract

Eight production quality PbWO_4 crystals of CMS have been irradiated in a 20 GeV/c proton beam up to fluences of $5.4 \times 10^{13} \text{ cm}^{-2}$. The damage recovery in these crystals has been followed for over a year. Comparative irradiations with ^{60}Co photons have been performed on seven other crystals using a dose rate of 1 kGy/h. In proton irradiated crystals the light transmission band-edge shifts and the induced absorption length $\mu_{\text{IND}}(\lambda) \propto \lambda^{-4}$. In γ -irradiated crystals the band-edge does not shift but formation of absorption bands is seen clearly. The absorption length induced by γ -radiation in crystals verified to have excellent radiation hardness, saturates at a level below 0.5 m^{-1} . In the case of protons, we observe no correlation with the pre-characterised radiation hardness of the crystals and the induced absorption increases linearly with fluence. After a fluence of $5 \times 10^{13} \text{ cm}^{-2}$, an induced absorption length of $\sim 15 \text{ m}^{-1}$ is seen with no sign of saturation. These observations provide strong evidence that high-energy protons create damage that cannot be reproduced with γ -irradiation. However, these hadronic effects manifest themselves only at integral fluences well beyond 10^{12} cm^{-2} and most likely would escape undetected at lower fluences. A large fraction of the damage, both in proton- and γ -irradiated crystals, is either stable or recovers very slowly.

1 Introduction

Lead Tungstate (PbWO_4) crystals will be used by several high-energy physics experiments [1, 2, 3] because they provide a compact homogeneous calorimeter with fast scintillation. In view of their use in the CMS experiment, where the calorimeters will face the harsh LHC conditions, the radiation hardness of PbWO_4 crystals has been extensively studied over the last decade [4, 5, 6, 7, 8, 9]. These studies have mostly been done at γ -irradiation facilities, complemented with some neutron tests at reactors [10]. At LHC, however, calorimeters will also be exposed to a large fluence of high-energy hadrons, resulting from up to $8 \times 10^8 \text{ s}^{-1}$ minimum bias pp interactions at $\sqrt{s}=14 \text{ TeV}$.

Although the radiation damage caused by minimum ionising particles in PbWO_4 has been thoroughly studied by the γ -irradiations, this cannot be considered sufficient for LHC applications. In particular, the fundamental difference between few MeV photons and energetic hadrons – the effects of nuclear interactions in the crystal – has not been investigated in detail so far. Some pion irradiations have been performed [11, 12] but no systematic study has been extended up to the full integrated hadron fluences expected at the LHC, although the necessity of this has been advocated long ago [13].

Inelastic nuclear interactions break up the target nucleus and thus create impurities and distortions in the crystal lattice. These effects, however, are expected to be negligible at LHC fluences, since the natural impurity concentration of the crystals is relatively high. Another unique feature of hadronic interactions is the very dense ionisation of the created heavy nuclear fragments, which can have a range of up to $10 \mu\text{m}$. Along their path they displace a large number of lattice atoms, but also ionise much more densely than a minimum ionising particle. In PbWO_4 the fragments with highest ionising dE/dx are known to come from fission of lead and tungsten where the cross section for such reactions exceeds 100 mb [14]. Typical fission fragments, like Fe and Zr in Fig 1, have energies up to 100 MeV . It can be seen from Fig. 1 that the dE/dx for such fragments is four orders of magnitude larger than for minimum-ionising protons – indicated by the solid dot in Fig 1. Since the thresholds to induce fission are several hundred MeV, tests with reactor neutrons or low-energy protons are not suitable to probe this regime.

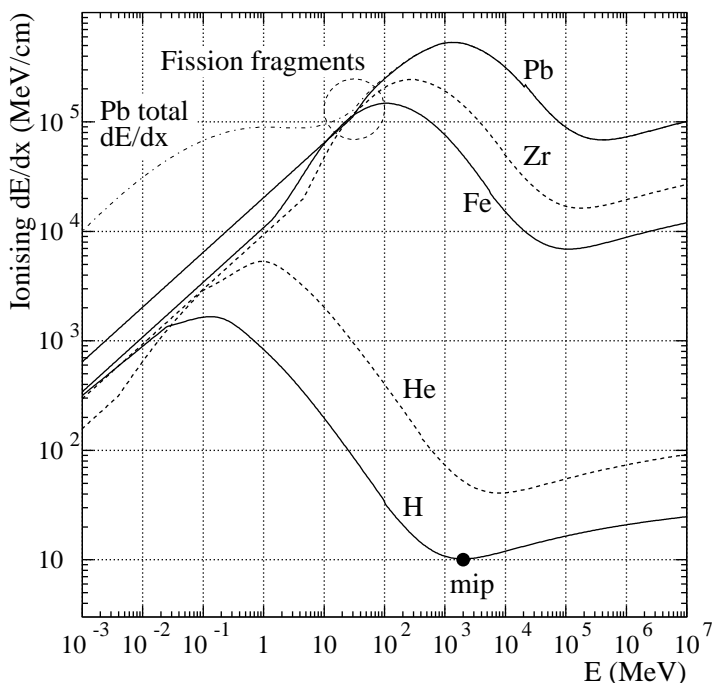


Figure 1: Simulated ionising energy loss of different fragments in PbWO_4 . Non-ionising energy loss is not included, but even for heavy fragments it is negligible above $\sim 10 \text{ MeV}$. This is quantified for lead fragments, where the total dE/dx is indicated by the dot-dashed line. The dashed circle shows the typical dE/dx -values of fission fragments at the beginning of their track.

An irradiation test of PbWO_4 with hadrons is more complicated than a standard γ -irradiation. The production of

Crystals for proton irradiations				Crystals for γ -irradiations		
ID	$\mu_{\text{IND}}^{\gamma\text{std}}(420)$	ϕ_p (cm ⁻² h ⁻¹)	t_{irr} (h)	ID	$\mu_{\text{IND}}^{\gamma\text{std}}(420)$	t_{irr} (h:min)
<i>a</i>	0.28	10 ¹²	1 + 10 + 50	<i>t</i>	1.22	27:20
<i>b</i>	0.79	10 ¹²	1	<i>u</i>	0.24	1:00
<i>c</i>	0.90	10 ¹²	1	<i>v</i>	0.25	46:00
<i>d</i>	0.39	10 ¹²	10	<i>w</i>	0.21	8:20
<i>E</i>	0.70	10 ¹³	1	<i>x</i>	1.6	8:20
<i>F</i>	0.55	10 ¹³	0.1 + 1	<i>y</i>	1.14	46:00
<i>G</i>	0.21	10 ¹³	0.1	<i>z</i>	1.96	1:00
<i>h</i>	0.50	5 × 10 ¹¹	20			

Table 1: List of all crystals, their initial radiation hardness pre-characterisation ($\mu_{\text{IND}}^{\gamma\text{std}}(420)$ in m⁻¹) based on the standard CMS γ -irradiation procedure [16]. t_{irr} is the exposure time in the proton beam with nominal flux ϕ_p or in the 1 kGy/h γ -facility, used in this work.

nuclear fragments causes the crystals to become radioactive, up to a level which does not allow handling them for several weeks after exposure. Any front-end electronics or optical system, like photomultipliers, laser or fibre is also susceptible to damage in the hadron beam and would make the determination of an effect in the crystal itself more complicated. Therefore our aim was to make the simplest possible test we could imagine. We irradiated bare crystals and measured the light transmission after irradiation. Our study was targeted at stable or very slowly recovering damage after a proton fluence of up to 5×10^{13} cm⁻².

2 The crystals

For our studies we used PbWO₄ crystals produced by the Bogoroditsk Techno-Chemical Plant (BTCP) in Russia for the electromagnetic calorimeter (ECAL) of the CMS experiment [1]. The crystals have the shape of truncated pyramids with nearly parallelepipedic dimensions of 2.4 × 2.4 cm² transversely and 23 cm length. All crystals were of production quality, and only because of slightly non-compliant mechanical dimensions or mild mechanical surface damage they could not be used in the ECAL construction. In particular, they were all pre-characterised for their radiation hardness through γ -irradiation at the Geneva Hospital ⁶⁰Co facility following a standard CMS qualification procedure. Throughout the paper we will refer to the results of this pre-characterisation as $\mu_{\text{IND}}^{\gamma\text{std}}(420)$.

The studies presented here concentrated on an examination of the change in longitudinal transmission (LT) at a wavelength of 420 nm, which corresponds to the peak emission of PbWO₄ scintillation light. The CMS technical specifications [15] require the radiation-induced absorption coefficient

$$\mu_{\text{IND}}(\lambda) = \frac{1}{\ell} \times \ln \frac{LT_0(\lambda)}{LT(\lambda)}, \quad (1)$$

at $\lambda=420$ nm to be below 1.5 m^{-1} for a saturated damage from γ -irradiation at ≈ 100 Gy/h. In Eq. 1 LT_0 (LT) is the longitudinal transmission value measured before (after) irradiation and ℓ is the crystal length (23 cm) through which transmission is measured.

For the proton irradiations we had 12 crystals at our disposal. In order to minimise the effect of crystal-to-crystal variations, we selected for our irradiation 8 crystals which showed the most consistent behavior in optical characteristics and in terms of $\mu_{\text{IND}}^{\gamma\text{std}}(420)$. The selected crystals are listed as *a–h* in Table 1.

For the γ -irradiations, performed at a dose rate corresponding to 10¹² p/cm², we used further 6 crystals, from a later production, which are listed as *u–z* in Table 1. The pre-characterisation of these 6 crystals was done for 1 h at 350 Gy/h which increases $\mu_{\text{IND}}^{\gamma\text{std}}(420)$ by about 10% [16] with respect to 2 h at 250 Gy/h, as used for the other crystals. Crystals *u*, *v* and *w* were of very good quality while the three others showed after the pre-characterisation quite high $\mu_{\text{IND}}^{\gamma\text{std}}(420)$ values. Two of them (*x* and *z*) were actually outside of the CMS specifications. In addition to these 6, one of those remaining from the earlier 12, was considered good enough to be used in the γ -irradiations and is labelled as *t* in Table 1.

The target dose rate in the γ -irradiations was 1–2 kGy/h but an exact analysis of the actual rate is presented later. Throughout this paper we use the convention to assign small letters to crystals irradiated at a dose rate of ~ 1 kGy/h and capital letters to those irradiated at rates of ~ 10 kGy/h. A prime or a double-prime after the crystal identifier indicates a second or third irradiation of the same crystal.

The t_{irr} times given in Table 1 for the proton irradiations are the target values but the actual fluences were determined by standard activation techniques. For the γ -irradiations, performed in static and very stable conditions, the t_{irr} values are the actual exposure times which are used in the dose determination.

3 Irradiations

For the proton irradiations we used the IRRAD1 facility [17] in the T7 beam line of the CERN PS accelerator, which at the time of our first irradiations was delivering a proton beam of 20 GeV/c and during a later campaign 24 GeV/c. In order to obtain a uniform irradiation over the whole crystal front face, we requested a special beam, which had not been produced before in that facility. In particular, we asked for the lowest beam intensity which the PS could provide in a controllable way in the T7 beam line.

At 20 GeV/c we obtained a flux of $\sim 10^{12} \text{ cm}^{-2}\text{h}^{-1}$ over an area of roughly $4.5 \times 4.5 \text{ cm}^2$. At 24 GeV/c a further intensity reduction by a factor of 2 was reached. The uniformity was not perfect over the whole beam spot, but a fairly uniform area covering the crystal could be found. In this low-intensity mode the PS was delivering on average one proton spill every 42 seconds. The duration of the spill was 600 ms at 20 GeV/c and 400 ms at 24 GeV/c.

In order to investigate a possible rate dependence, we performed some irradiations at a higher intensity, of $\sim 10^{13} \text{ cm}^{-2}\text{h}^{-1}$. To achieve this, the spill frequency was increased to 2 spills every 14 s and the beam spot was reduced to a size of about $3 \times 3 \text{ cm}^2$ which was still sufficient to cover the crystal while maintaining an acceptable beam uniformity.

The crystals were brought into the beam by a remotely controlled shuttle. The beam was hitting the small front face of the crystal and was parallel to the long crystal axis.

The γ -irradiations were performed at the Calliope plant of ENEA-Casaccia, Italy. The facility provides a ^{60}Co source which at the time of our irradiations had a total activity of 750 TBq. The 48 source rods were arranged in two concentric cylinders of about 20 cm outer radius and 26 cm height. We irradiated simultaneously up to 5 crystals, standing side-by-side at a distance of 40 cm from the source centre, with their long side parallel to the source axis. Each crystal was housed in its own styropor box. The distance between two adjacent crystals was about 34 mm. In order to obtain as uniform an exposure as possible, each box was turned once by 180° around its long axis at half-time through its exposure. Unfortunately the crystals could not be precisely adjusted with respect to the source and an offset of 52 mm remained along the axis. Thus one extremity of the crystals was slightly less exposed.

4 Measurement methods

4.1 Light transmission

The LT measurements were taken with a Perkin Elmer Lambda 900 spectrophotometer for wavelengths between 300 and 800 nm in 1 nm steps. Since the grating which allows to select the desired wavelengths polarises light, we used a wide-band depolariser to be reasonably free of polarisation effects. The width of the beam is defined by the slit opening which fixes the wavelength distribution: this we set to $\Delta\lambda = 1 \text{ nm}$ which yields about 7 mm beam size. The height was adjusted with a “common beam mask” to approximately 10 mm.

We will discuss later the implications of non-uniform proton beam profiles, which required us to align the crystals in a reproducible way. For each measurement we checked that the entry and exit points of the light were centred on the crystal face. The accuracy of this alignment was roughly $\pm 1 \text{ mm}$. Measurements with intentionally larger displacements showed this to be sufficiently good not to introduce significant variation for any of our crystals.

For each proton-irradiated crystal, at least one set of LT measurements was performed, where the light was passed not only through the centre, but also as close to each of the four sides as possible. The information gained from these “scans” served the purpose of understanding effects of beam non-uniformities.

Before each session of measurements we experimentally verified the absolute calibration of the device by measuring the LT of a non-irradiated reference crystal. Fig. 2 shows the results of these measurements as a function of time at 420 nm. From the scatter of the points we derive a 1σ deviation of 0.58%. However, close to the band-edge the transmission changes rapidly and the accuracy of the wavelength dominates. We were able to reproduce the scatter of the reference crystal LT close to the band edge, if we assumed that the wavelength is reproduced with

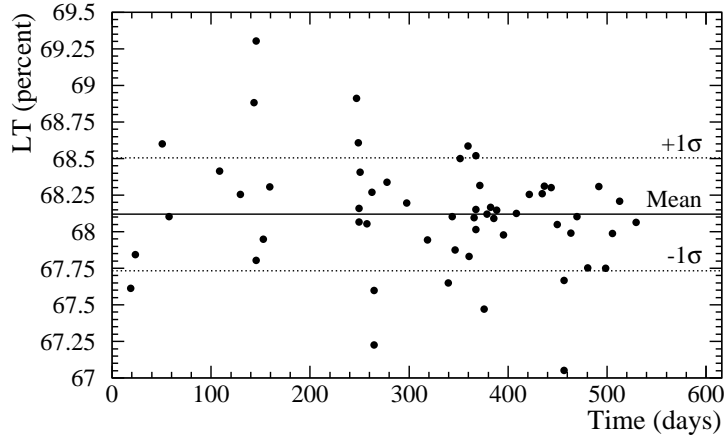


Figure 2: LT data measured on the reference crystal at 420 nm. The 0-point of the time axis is arbitrary, but the relative time intervals correspond to real elapsed time.

0.23 nm accuracy. Thus we estimate the total error of the LT measurement at wavelength λ as

$$\Delta[LT(\lambda)] = 0.0058 \times LT(\lambda) \oplus 0.23 \times \delta_{LT(\lambda)}, \quad (2)$$

where $\delta_{LT(\lambda)}$ is the difference between two adjacent LT points, 1 nm apart. The second term is significant only close to the band edge, when $\delta_{LT(\lambda)}$ can be as big as three percent-units per nm. At large wavelengths, when the transmission changes slowly with λ , the error is given by the first term alone.

4.2 Induced radioactivity

The induced radioactivity dose rate (\dot{D}_{ind}) was measured with an Automess 6150AD6 [18] at a distance of 4.5 cm from the long face of the crystal at its longitudinal centre. The device was calibrated to yield the photon equivalent dose, which is the quantity extracted from the simulations described in appendix A.

The reference point of the sensitive element in the 6150AD6 is reported to be 12 mm behind the entrance window. Thus our actual distance was 57 mm from the crystal face. The \dot{D}_{ind} values of the least active crystals were comparable to natural background, which we determined by integrating over a long period with the 6150AD6. In order to verify the linearity of the device even at low counting rates, we also measured the dose from a standard point-like ^{137}Cs source at various distances. Both methods gave a background of $0.06 \mu\text{Sv/h}$ and we observed no dependence on counting rate.

The nominal energy range of the 6150AD6 is 60 keV–1.3 MeV. Below 60 keV the efficiency drops abruptly, but in our crystals only a negligible fraction of dose comes from low energy photons. The efficiency curve [18], which rises steeply above 1 MeV, is cut at 1.3 MeV, which marks the end of the calibrated range. Our assumption of constant efficiency above this energy most likely leads to an underestimate of our simulations with respect to the measured values.

Since PbWO_4 attenuates photons quite efficiently, a measurement of \dot{D}_{ind} provides a means to approximately determine the proton beam uniformity. For this purpose \dot{D}_{ind} was measured on all long sides for each crystal. Although the attenuation is exponential, a simple average over the four sides gives the total activation with an accuracy of a few percent even for our most non-uniform irradiations.

All \dot{D}_{ind} measurements were prolonged sufficiently to reduce the statistical uncertainty to the level of 1–2%.

5 Simulation of the irradiation conditions

5.1 Proton beam

Since the crystals are longer than one hadronic interaction length, the protons initiate an intense hadronic cascade. In addition, the irradiation zone is a fairly small volume with steel walls on 4 sides at distance of few tens of

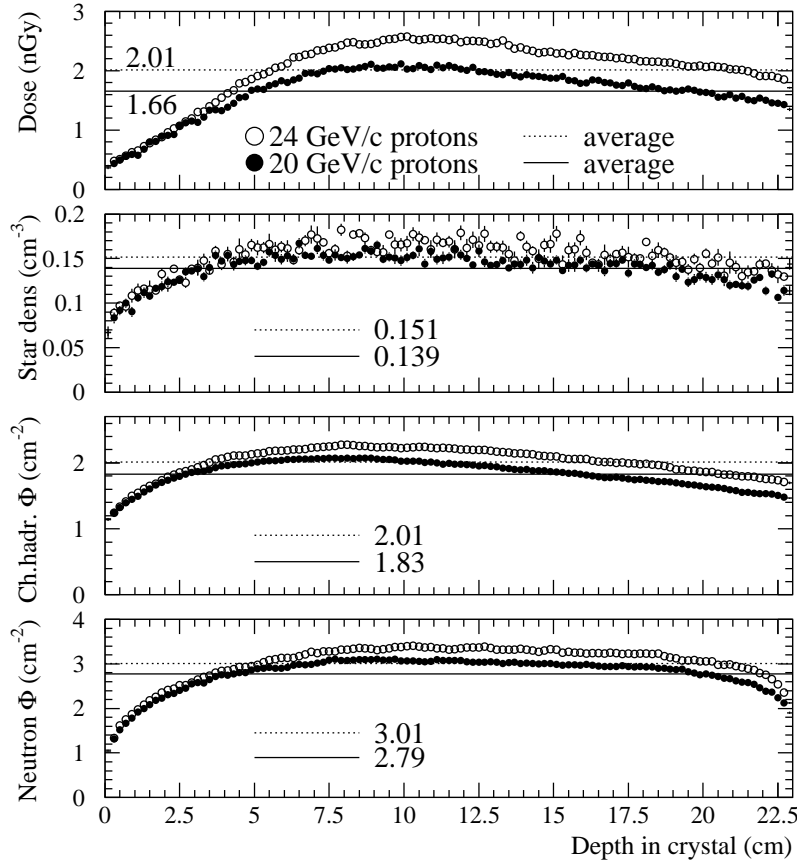


Figure 3: Ionising dose, star density, charged hadron and neutron fluences per unit of incident proton fluence as obtained from the simulations. Values are for a $5 \times 5 \text{ cm}^2$ proton beam of 20 GeV/c (solid dots and lines) or 24 GeV/c (open dots, dashed lines). The lines and associated values give the average over the whole crystal length in the central area, covered by the light beam in the LT measurements.

	Beam protons	>20 MeV protons	>20 MeV pions	>20 MeV neutrons
Front	0.997	1.056	0.041	0.163
Rear	0.390	0.764	0.497	0.536

Table 2: Simulated hadron fluxes (cm^{-2} per unit of incident flux) in the first and last millimetre of the 23 cm long crystal hit by a 20 GeV/c proton beam.

centimetres. The back wall is in fact the beam dump of the T7 beam line. Thus the possible effects of back-scattered radiation cannot be ignored.

In order to properly understand the radiation field within and around the crystal – and in particular the influence on the determination of the incident proton fluence – a full simulation of the irradiation setup was performed with the FLUKA code [19]. For the simulations, the crystal shape was described as a 23 cm long truncated equal-sided pyramid with a minor face of $22 \times 22 \text{ mm}^2$ and a major face of $26 \times 26 \text{ mm}^2$. The main quantities characterising the radiation field, as obtained from these simulations, are shown in Fig. 3.

Damage caused by γ -irradiation is found to saturate at a level corresponding to the dose rate used [20]. However, since we are looking for the possible existence of cumulative damage¹⁾ specific to hadrons, it seems more

¹⁾ Earlier hadron irradiations reported in [11, 12] did not show any difference between γ and pion irradiation performed at the same rate. But these tests cannot be considered sufficient to exclude possible cumulative effects because they were not extended to high enough fluences.

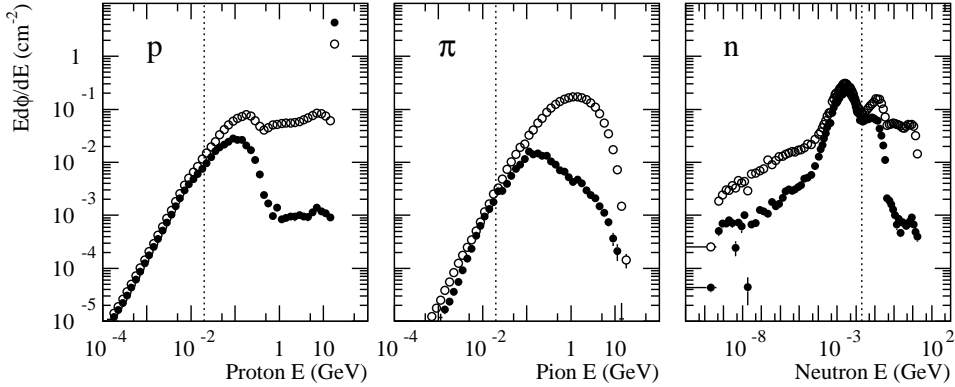


Figure 4: Energy spectra of protons, charged pions and neutrons in the first (solid circles) and last (open circles) millimetre of a 23 cm long crystal. The dotted line shows the 20 MeV threshold above which hadrons can produce stars.

appropriate to use, instead of dose rate, a purely hadronic quantity against which we could plot the damage.

The incident proton beam is practically monoenergetic but, due to cascade formation, the hadron spectrum within the crystal, shown in Fig. 4, comprises all energies from sub-MeV neutrons to full beam energy. Table 2 shows the integral fluences at beam energy and above 20 MeV – the threshold indicated by the dashed lines in Fig. 4. With such a wide energy spectrum and since a dependence between damage and hadron energy cannot be excluded *a priori*, it is not obvious how damage could be related to hadron fluence.

It is plausible that any damage unique to hadrons should be caused by the component of the hadron spectrum which is producing inelastic interactions. The most suitable quantity to describe the radiation field for our purpose, is called *star density*, which was originally introduced to parametrise radioactivity induced by hadron irradiation [21]. A *star* is defined as an inelastic hadronic interaction caused by a projectile above a given threshold energy. This means that the star density is actually the integral of the total hadron fluence above a given threshold, weighted by the inelastic cross section. The star density is exactly zero for irradiations with low energy photons or neutrons below the threshold energy, which we take as 20 MeV. For constant beam conditions the star density is of course proportional to the fluence. In our analysis we will prefer the latter because it can be experimentally determined with good accuracy. The simulated star densities, however, will be used to scale between different beam energies and to compare different radiation environments.

Since the radioactivity produced in the crystal is roughly proportional to the rate at which stars are produced [22], a measurement of \dot{D}_{ind} in a crystal can provide an estimate of the star density. This is discussed in more detail in appendix A.

5.2 ^{60}Co source

The dose rates at the Calliope plant [23] are well known from measurements, performed regularly by the operators. However, these values refer to dose in air or water in the absence of scattering material. In order to determine the dose profile within the crystals, detailed simulations of the irradiation setup were mandatory. Fig. 5 shows the FLUKA simulation model of the source and 5 crystals in their boxes. Since durations of irradiations were different, not all positions were occupied at all times. Due to these changes in configuration and the slightly different position with respect to the source, the dose in individual crystals is slightly different.

As in the case of proton irradiated crystals, we again determine the transmission along the long axis of the crystal, and therefore we are interested in the dose along the centre. Fig. 6 shows the simulated transverse dose rate profiles, which exhibit a pronounced U-shape, caused by turning the crystal half-way through the irradiation. The fairly flat central part, of about ± 5 mm width, fits very well the width of the light beam in the LT-measurements. In the other dimension the profile is flat.

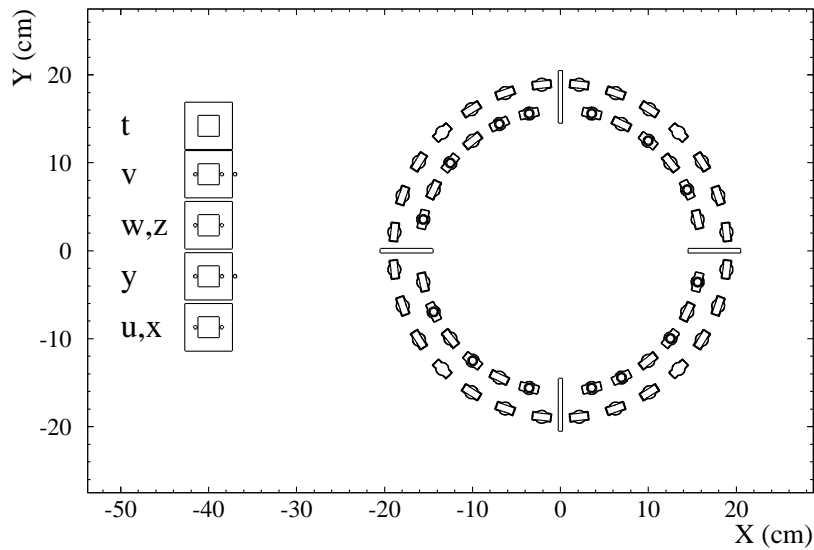


Figure 5: Top view of the simulation geometry representing the Calliope facility. The two concentric assemblies of source rod rings are seen on the right and the 5 crystals inside their boxes on the left. The positions of each crystal are indicated by their identifiers next to the boxes. The small dots on and within the crystal boxes represent alanine dosimeter positions.

Figure 7 shows the simulated longitudinal dose rate profile along the long axis of the crystal. The dose drops quite significantly towards the end of the crystal because the height of the source could not be exactly aligned with the crystals. The discontinuities, e.g. the step at 18 cm for crystal *w*, are caused by the support structures of the source

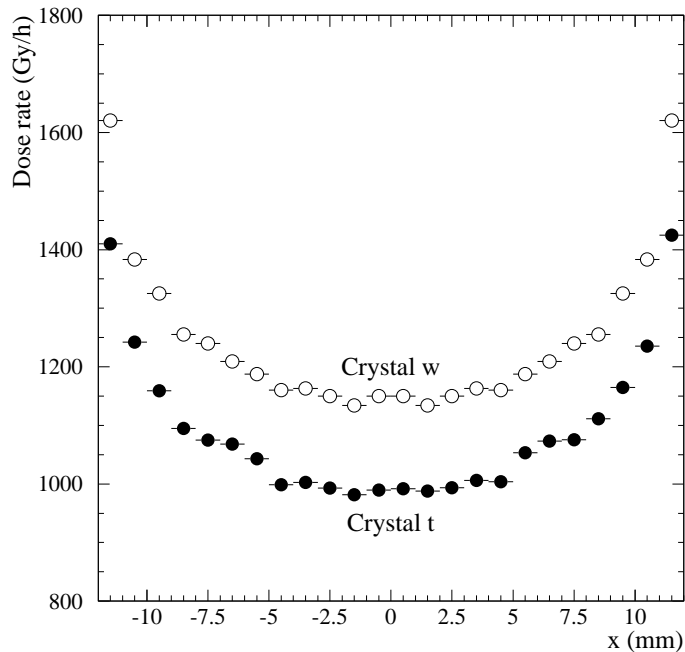


Figure 6: Simulated transverse dose rate profiles in the crystals. Shown are the minimum (crystal *t*) and maximum (crystal *w*) dose rates in the 7 crystals. The profiles represent an average over the whole length of the crystal.

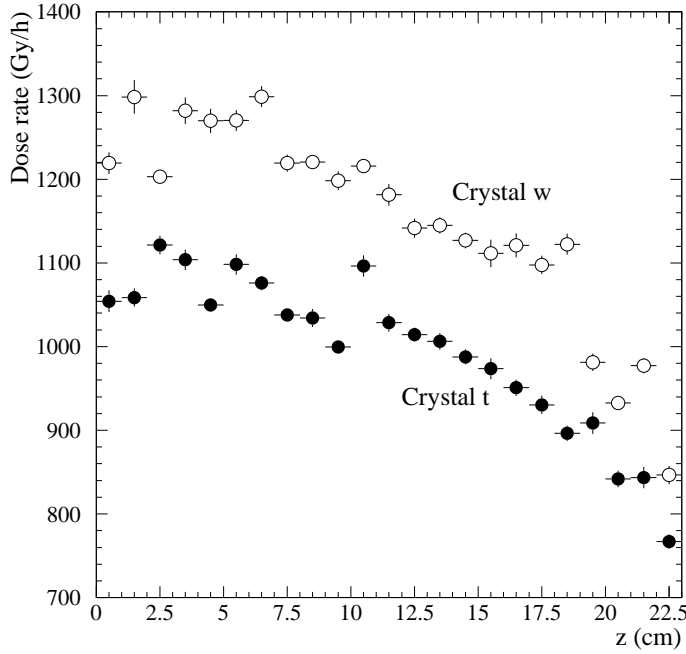


Figure 7: Simulated longitudinal dose rate profiles along the centre of the crystals (± 5 mm around central axis). Shown are the minimum (crystal *t*) and maximum (crystal *w*) dose rates in the 7 crystals.

assembly.

6 Fluence and dose determination

6.1 Proton fluence determination in IRRAD1

The fluence, Φ_p , of the incident proton beam was determined with aluminium foils, cut to a size of 24×24 mm² and placed in front of the crystals at a distance of about 10 mm. Secondaries produced by the crystals, neutrons in particular, influence this measurement. Therefore we preferred to use the isotope ²²Na instead of the more standard ²⁴Na. The determined fluence, in particular its relation to the star density within the crystal, is sensitive to the geometry and alignment. A further factor to be taken into account came from a change of beam momentum from the initial 20 GeV/c to 24 GeV/c. Therefore we paid great attention to a careful fluence analysis and cross checks with the induced radioactivity in the crystal itself. The technical aspects of this and all effects considered, together with the correction factors derived by us, are detailed in appendix B.

Table 3 summarises the proton fluences and gives the dose rates and total doses averaged along the axis of the crystal. The first column, $\Phi_p(^{22}\text{Na})$, gives the fluence value obtained from the aluminium foils but corrected by the factor of 0.89 in order to account for activation by secondaries. The $\sum \Phi_p$ -column gives the integral of all subsequent irradiations for a given crystal and also includes the correction by a factor of 1.086 to account for the higher beam energy in the case of crystals *a*'' and *h*. Any quantity that is cumulative and stable, should appear proportional to $\sum \Phi_p$.

The dose values given in Table 3 correspond to an average along the axis of the crystal, i.e. along the path of light in the LT measurements. Averaging was done over the dimensions of the light beam. It can be seen from Fig. 3 that in the proton irradiations the maximum dose rate, at a depth of about 10 cm within the crystal, is $\sim 30\%$ above this average.

One issue which will be discussed in detail in appendix C is the uniformity of the beam spot across the crystal face. These effects, however, remained small enough to require no corrections. Actually, as shown in appendix C, the simulated effects of non-uniform irradiation agree nicely with measured variations of \dot{D}_{ind} and LT close to the edges of the crystal.

ID	$\Phi_p(^{22}\text{Na})$ (cm^{-2})	$\sum \Phi_p$ (cm^{-2})	Dose rate (kGy/h)	Dose (kGy)
b	$(0.46 \pm 0.03) \times 10^{12}$	$(0.46 \pm 0.03) \times 10^{12}$	0.99	0.77
c	$(0.74 \pm 0.05) \times 10^{12}$	$(0.74 \pm 0.05) \times 10^{12}$	1.40	1.23
a	$(1.01 \pm 0.11) \times 10^{12}$	$(1.01 \pm 0.11) \times 10^{12}$	1.06	1.67
F	$(1.37 \pm 0.16) \times 10^{12}$	$(1.37 \pm 0.16) \times 10^{12}$	22.8	2.28
G	$(1.72 \pm 0.18) \times 10^{12}$	$(1.72 \pm 0.18) \times 10^{12}$	28.5	2.85
E	$(7.66 \pm 0.55) \times 10^{12}$	$(7.66 \pm 0.55) \times 10^{12}$	15.9	12.7
h	$(8.70 \pm 1.00) \times 10^{12}$	$(9.46 \pm 1.09) \times 10^{12}$	0.66	17.4
F'	$(8.46 \pm 0.85) \times 10^{12}$	$(9.83 \pm 0.86) \times 10^{12}$	18.0	16.3
d	$(12.0 \pm 1.2) \times 10^{12}$	$(12.0 \pm 1.2) \times 10^{12}$	1.74	20.0
a'	$(12.2 \pm 1.0) \times 10^{12}$	$(13.2 \pm 1.1) \times 10^{12}$	1.66	21.9
a''	$(37.6 \pm 2.3) \times 10^{12}$	$(54.1 \pm 2.7) \times 10^{12}$	1.25	97.5

Table 3: Proton fluences $\Phi_p(^{22}\text{Na})$ for each individual irradiation as obtained from the Al-activation and cumulative fluences ($\sum \Phi_p$) for a given crystal. The latter also includes the correction for beam energy (see text). The last two columns give the average ionising dose rate and integral dose along the axis of the crystal. The dose values are based on simulations, renormalised to the measured fluence at proper beam energy.

6.2 Dose determination at the γ -facility

Alanine dosimeters provide a well-established method to determine cumulative ionising doses. The absolute calibration is usually done with a standard ^{60}Co source and converted to give the dose in air. Ten alanine dosimeters which accompanied the irradiations provided a crucial cross-check of our dose simulations. Six of these dosimeters were fixed on the “front” of each of the crystals u – z , i.e. the side facing the source, while two were on the “back” of crystals v and y . When turning the crystals, “front” and “back” got inverted so that each of these eight alanines was averaging equally over the “front” and “back” of a crystal. A further two dosimeters were fixed on the source side of the styropor boxes housing crystals v and y . These dosimeters were removed when the boxes were turned after the first 23 hours of exposure. All 10 alanines were included in the simulations and the dose in them was recorded. Figure 8 shows a comparison between the doses determined from the alanines and the simulated values. While the low doses of the 1 h and 8.3 h irradiations are in perfect agreement, alanines exposed for the longest times indicate a lower value than the simulations. Due to the symmetry of the simulated setup – essentially the same result was just rescaled with time – it is inconceivable that the simulation would fail for higher doses. The response of alanine is usually quoted to be linear up to about 100 kGy. However, when approaching the upper limit, saturation sets in gradually. Although saturation is taken into account in the calibration [24], an explanation

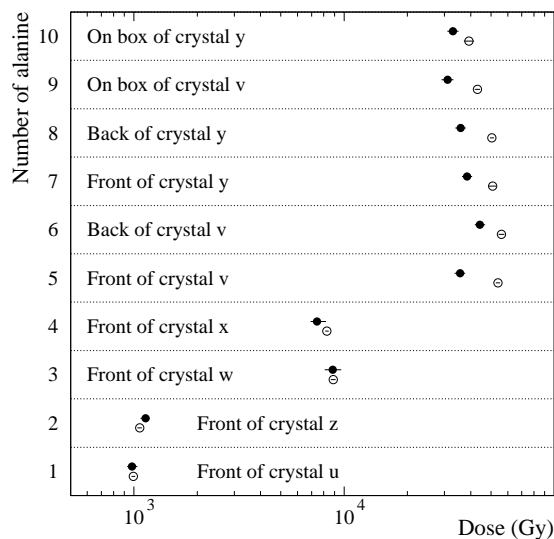


Figure 8: Simulated (open circles) and measured (solid circles) cumulative doses in the 10 alanine dosimeters exposed during our γ -irradiations.

ID	Dose rate (kGy/h)	Dose (kGy)
u	1.02	1.02
z	1.15	1.15
x	1.02	8.49
w	1.15	9.59
t	1.00	27.3
y	1.06	48.9
v	1.09	50.3

Table 4: Dose rates and cumulative doses reached in the γ -irradiations. Values are averages over the crystal length along the centre axis. The statistical errors are smaller than 1%.

for the difference observed could still be if saturation depends also on the photon energy spectrum, which is softer in the presence of the crystal than for a plain ^{60}Co calibration source.

Table 4 summarises the doses and dose rates reached in the γ -irradiations. These values have been extracted directly from the simulation described in section 5.2 but their accuracy has been experimentally verified by the comparison with the alanine data, shown in Fig. 8. The dose rate at one end was about 10% higher than the average and dropped to 20% below average at the other end of the crystals, as can be seen in Fig. 7.

7 Results

Fig. 9 shows typical LT curves of a non-irradiated crystal and of some crystals which have suffered radiation damage in the proton beam. With increasing $\sum \Phi_p$, not only the transmission worsens, especially in the blue region of the spectrum, but in addition the LT band edge shifts towards higher wavelengths. At $\sum \Phi_p \approx 10^{13} \text{ cm}^{-2}$ this shift starts to increasingly cut into the intrinsic emission spectrum of the crystal.

Fig. 10 shows the transmission curves as a function of wavelength for all 7 crystals irradiated with ^{60}Co photons. The shapes of the LT curves of γ -irradiated crystals are completely different from those of proton-irradiated ones. Even after the highest cumulative dose reached, the band-edge in γ -irradiated crystals does not shift at all, thus

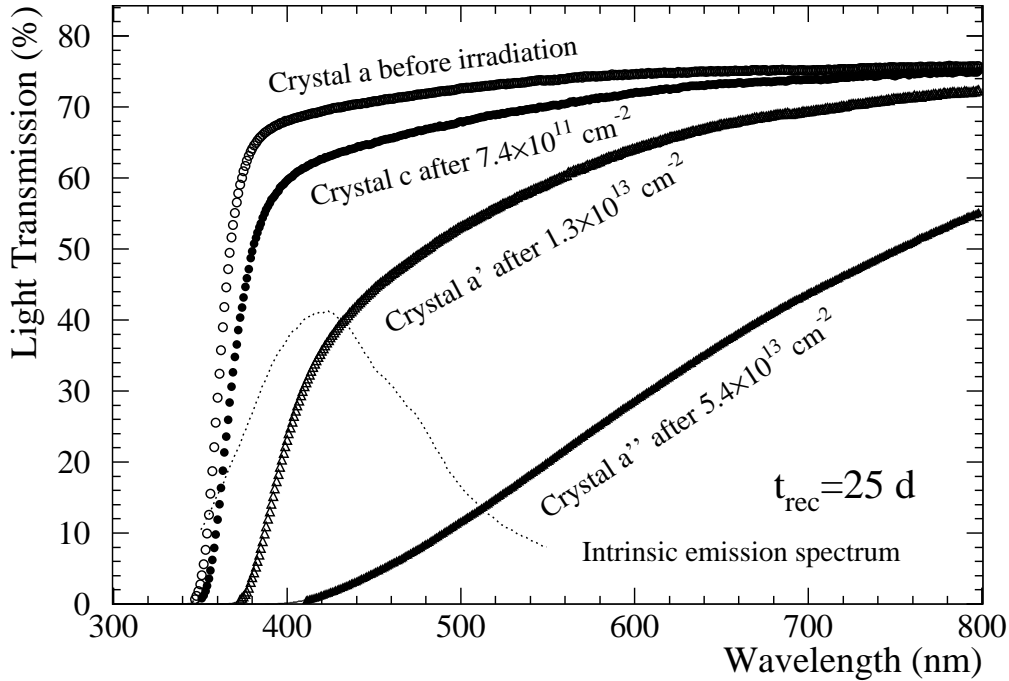


Figure 9: LT curves for crystals with various degrees of proton induced radiation damage. The emission spectrum (dotted line) is taken from [25] and has arbitrary normalisation.

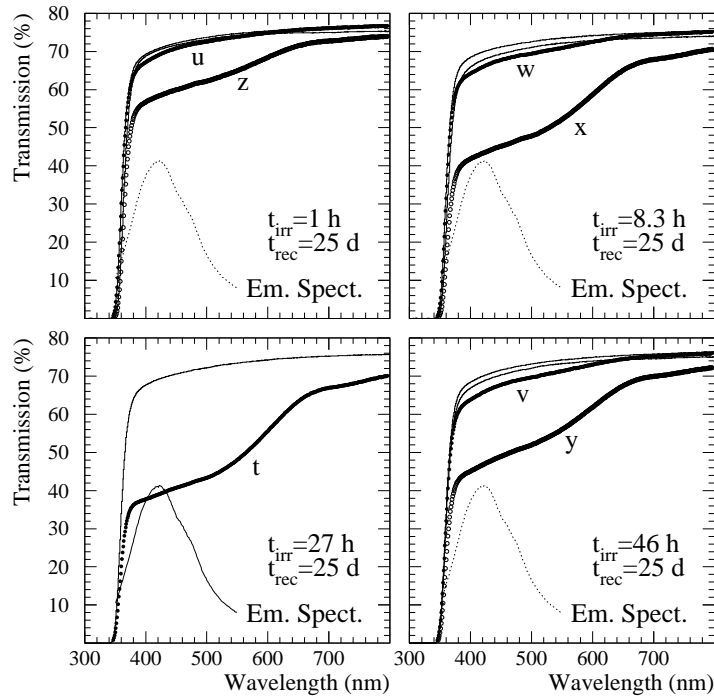


Figure 10: LT curves for crystals with various degrees of γ -induced radiation damage. The lines show the light transmission prior to irradiation. The order of these curves is the same as of the post-irradiation ones. The emission spectrum (dotted line) is taken from [25] and has arbitrary normalisation.

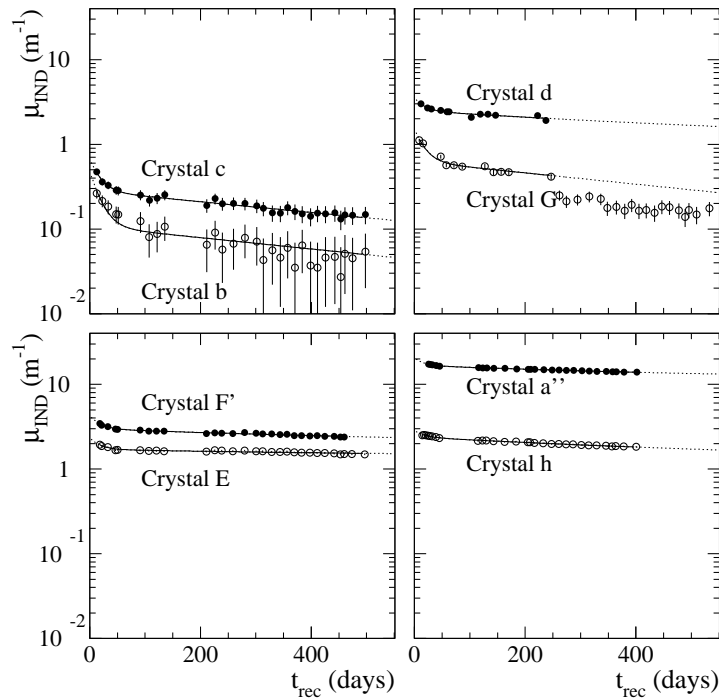


Figure 11: The fits of Eq. 3 to recovery data of our proton irradiated crystals. The last points of crystal G are excluded from the fit – see text.

establishing a fundamental difference between the damage caused by protons and the one caused by purely ionising radiation. Instead, one recognizes the absorption band around 420 nm, which is typical for γ -irradiated BTCP crystals [5]. Although this band is probably also present in proton-irradiated crystals, it does not appear in the LT

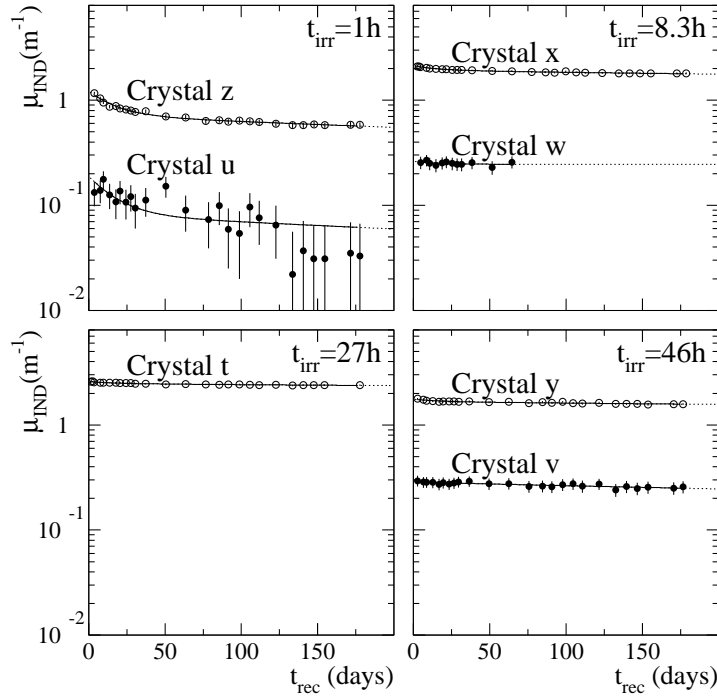


Figure 12: Recovery data of crystals irradiated with ^{60}Co photons up to various cumulative doses at a dose rate of ~ 1.1 kGy/h.

curves as a main feature of the damage. Furthermore, in γ -induced damage we see a significant crystal-to-crystal variation. This agrees well with the variation of the $\mu_{\text{IND}}^{\gamma\text{std}}(420)$ values in Table 1. No significant correlation of this kind is seen in the proton-irradiated crystals.

7.1 Recovery time constants

We fit the time dependence of μ_{IND} with a sum of two exponentials and a constant

$$\mu_{\text{IND}}(420, t_{\text{rec}}) = \sum_{i=1}^2 A_i \exp\left(-\frac{t_{\text{rec}}}{\tau_i}\right) + A_3, \quad (3)$$

where t_{rec} is the time elapsed since the irradiation. Attempts to fit Eq. 3 for each crystal, with all 5 parameters free, revealed that the longer time constant (τ_2) was comparable to, or larger than, t_{rec} and thus the correlation between the second term and the constant was too strong to allow for a reliable fit. It is, however, reasonable to assume that the damage corresponds to the same color centres, each of which corresponds to a unique time constant. Under this assumption we fitted the τ_i for all crystals simultaneously and, with these fixed, the amplitudes A_i for each crystal separately. This process was iterative, i.e. τ_i and A_i were fitted repeatedly with increasingly better initial guesses until convergence was reached. The quality of the fits, in terms of χ^2 , was comparable to that obtained by the 5-parameter fit of Eq. 3 for each crystal separately.

Figs. 11 and 12 show the fits for proton and γ -irradiated crystals, respectively. In comparison to the observed recovery time constants, crystals a , a' and F were re-irradiated too soon and therefore do not allow to obtain reasonable fits.

Of the proton irradiated crystals, d was annealed 240 days after irradiation, thus we have no longer-term room temperature recovery data for it. While essentially no recovery of crystal d was observed at 160 °C, partial recovery took place at 250 °C. This temperature was sufficient to restore the pre-irradiation transmission at $\lambda > 400$ nm. At a temperature of 350 °C almost complete recovery was reached, except for a small residual shift of the band-edge.

In the case of crystal G a peculiar step appeared after 250 days, which we traced back to an unintentional exposure to normal room light from fluorescent tubes for about 60 hours during a long radioactivity measurement. The existence of such light-induced annealing was qualitatively verified by exposing to the same room lights a crystal

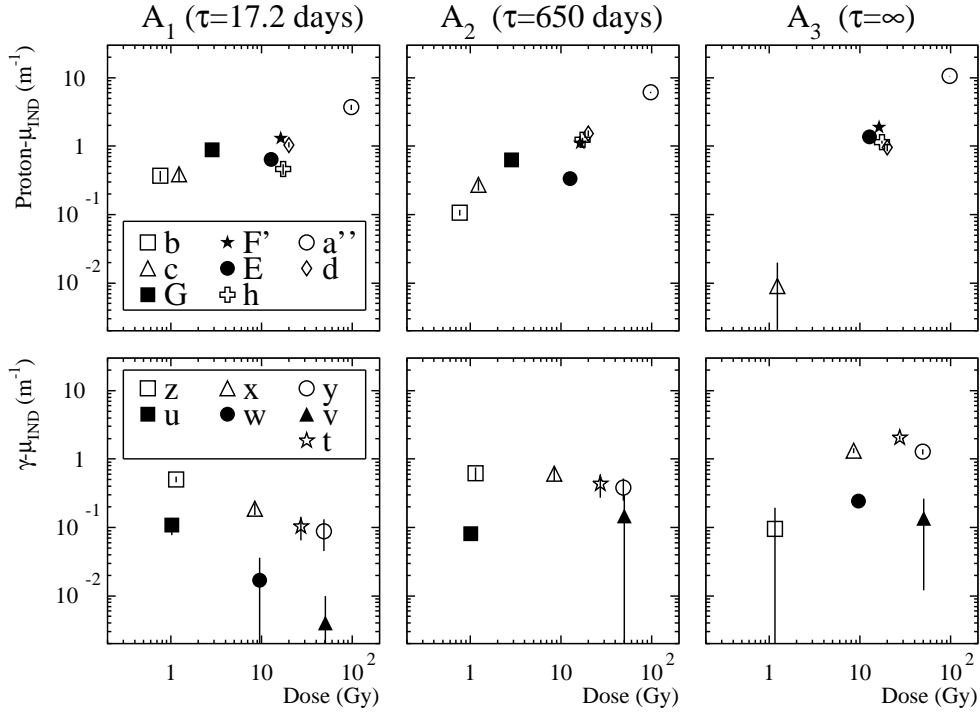


Figure 13: The amplitudes A_i of Eq. 3 as a function of dose. The dose to fluence correspondence for the proton-irradiated crystals can be found in Table 3. When symbols are not present in the plot, the fitted amplitude for that crystal is consistent with zero.

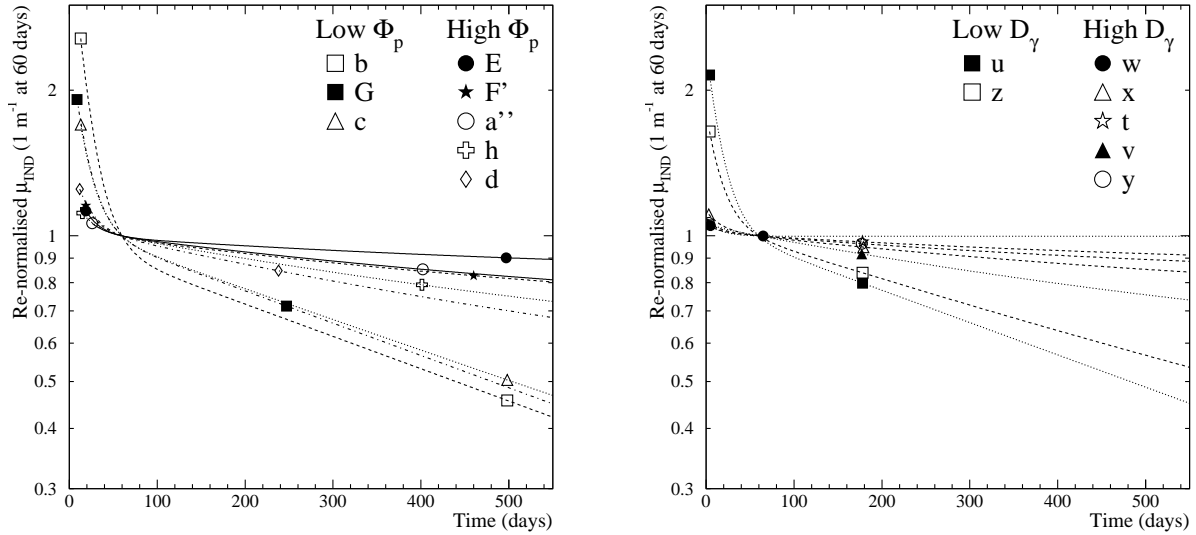


Figure 14: Plots of Eq. 3 with the parameter values shown in Fig. 13 after renormalisation to unity at $t=60$ days. The symbols indicate the range over which data were available for a given crystal.

that had been proton irradiated while exercising the procedures for this work. The very severe damage in that crystal had remained stable for almost 2 years but about 15% of it annealed fairly rapidly under light exposure.

The γ -irradiated crystal w was annealed 65 days after irradiation, in preparation for a later proton irradiation.

From the global fit we obtained $\tau_1=17.2$ days and $\tau_2=650$ days. The amplitudes corresponding to these recovery

time constants are shown in Fig. 13. The amplitude corresponding to τ_1 is slightly increasing with dose in the case of proton irradiation while it decreases as a function of γ -dose. This decrease could be due to the longer-lived defects, which build up and contribute to light attenuation, making A_1 relatively less effective. Since τ_2 was fitted to a value of 650 days, which is longer than the period of the recovery follow-up, the amplitudes A_2 and A_3 could not be reliably resolved from each other. This was particularly true for all γ -irradiated crystals and proton irradiated crystals d and G , where recovery data extends only to $t_{\text{rec}} \sim 200$ days. However, the sum of $A_2 + A_3$ for the proton irradiated crystals increases linearly with fluence, while it is consistent with a constant for γ -irradiated crystals.

All fits – re-normalised to the same values at $t_{\text{rec}}=60$ days – are shown in Fig. 14. Re-normalisation at 60 days was chosen such that the τ_1 -component of damage has practically disappeared. Thus the left side of the re-normalisation point shows the relative amplitude of the damage corresponding to τ_1 , while the right side provides a visual comparison of the magnitude of the long-term damage. Especially in terms of the short component the crystals group according to the integral fluence or dose they received. Those exposed to $\sum \Phi_p \sim 10^{12} \text{ cm}^{-2}$ (or $\sim 1 \text{ kGy}$) recover, in relative terms, more than those irradiated to higher fluence. While a slight difference between proton- and γ -irradiated crystals can be seen in the magnitude of the fast component, the long term recovery appears to be independent of the radiation type.

7.2 Correlation between light transmission and $\sum \Phi_p$ or γ -dose

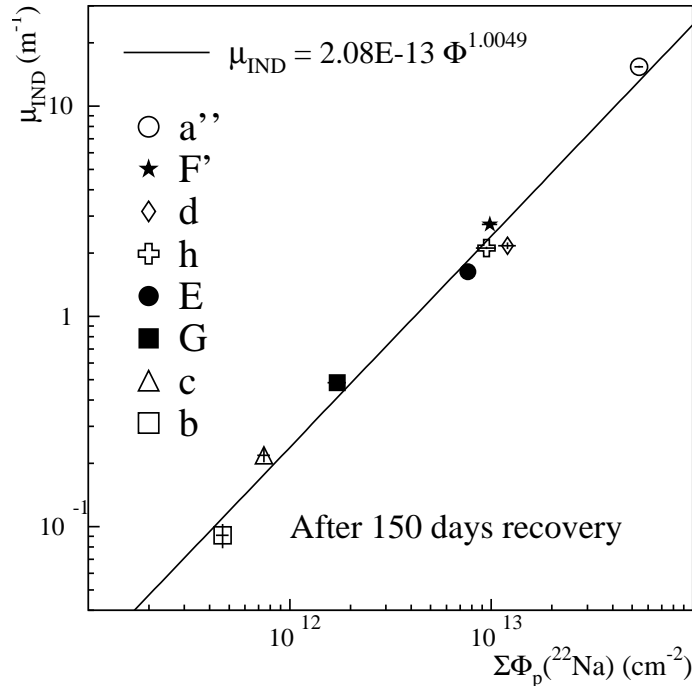


Figure 15: Induced absorption $\mu_{\text{IND}}(420)$ as a function of cumulative proton fluence.

Figure 15 shows $\mu_{\text{IND}}(420)$ as a function of fluence 150 days after irradiation as calculated from Eq. 3 using the parameter values shown in Fig 13.

For crystals irradiated several times, the cumulative fluence $\sum \Phi_p$ has been used and $\mu_{\text{IND}}(420)$ has been normalised to the transmission before the first irradiation. We have fitted the data, which cover two orders of magnitude, on a log-log scale and obtain an exponent that corresponds to only 1% deviation from linearity per order of magnitude in fluence. In particular, if the data in Fig. 15 are compared with Table 1, no correlation between proton-induced damage and $\mu_{\text{IND}}^{\gamma\text{std}}(420)$ can be observed.

Fig. 16 confirms that even at a dose rate as high as 1 kGy/h the γ -damage saturates. After 1 hour at 1 kGy/h, $\mu_{\text{IND}}(420)$ has not yet reached its plateau value, but between 8.3 and 46 hours the differences observed can be entirely attributed to crystal-to-crystal variation. This becomes particularly clear when we normalise $\mu_{\text{IND}}(420)$,

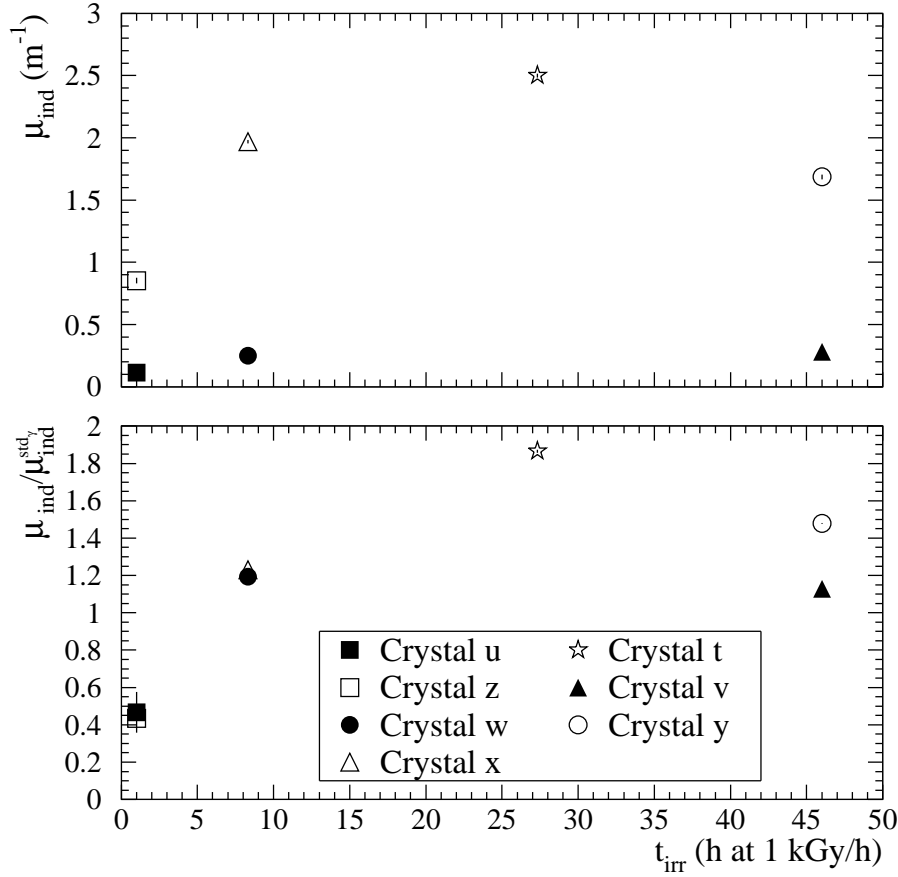


Figure 16: Values of $\mu_{IND}(420)$ measured on the 7 γ -irradiated crystals after 20 days recovery at room temperature. The upper plot shows the measured data and the lower one the ratio to the $\mu_{IND}^{\gamma std}(420)$ -values from Table 1.

as measured by us, with the $\mu_{IND}^{\gamma std}(420)$ -values from Table 1, which is supposed to cancel any crystal-to-crystal variation. It should be noted, however, that the $\mu_{IND}^{\gamma std}(420)$ values are obtained only about 1 hour after irradiation, i.e. before short-term recovery is completed. In fact, it has been observed that about 60% of the damage contributing to $\mu_{IND}^{\gamma std}(420)$ recovers during the first 20 days while the rest is much more stable [16]. If this is taken into account in the $\mu_{IND}(420)/\mu_{IND}^{\gamma std}(420)$ ratio of Fig. 16, the 1 h points are nearly consistent with unity while the ratios for longer irradiations get pushed to a value of about 3. This large ratio is at least partly – maybe even mostly – due to the fact that the pre-characterisation irradiations did not last long enough to saturate all color centres.

Crystal *t* shows slightly higher $\mu_{IND}(420)$ values than the other 6 crystals in Fig. 16. The deviation is even more pronounced in the $\mu_{IND}(420)/\mu_{IND}^{\gamma std}(420)$ ratio. These differences might well be, because *t* is from the earlier set of 12 crystals received for the proton tests. These had undergone a different pre-characterisation procedure almost a year earlier. While the 10% difference in $\mu_{IND}^{\gamma std}(420)$, due to the different dose rate, has been taken into account, there could still be other systematic or procedural effects that might have led to a slightly lower $\mu_{IND}^{\gamma std}(420)$ of crystal *t*.

When comparing the data of Figs. 15 and 16, it should be taken into account that the proton irradiated crystals all had $\mu_{IND}^{\gamma std}(420) < 1 m^{-1}$ and most of them should be compared with the solid symbols in the upper plot of Fig. 16. In particular, as can be seen from Table 1, crystal *a*” was characterised as having the same, excellent, radiation hardness as crystal *v*. After exposure to comparable integral doses, the proton irradiated crystal *a*” shows an induced absorption of $15 m^{-1}$ while the γ -irradiated crystal *v* has saturated at a value of only $0.3 m^{-1}$.

The shape of the LT curves, in particular the shift of the band-edge after proton exposure and the fact that two universal time constants fit the data well but give very different dose-dependence for the amplitudes in Eq. 3, leads us to the following interpretation:

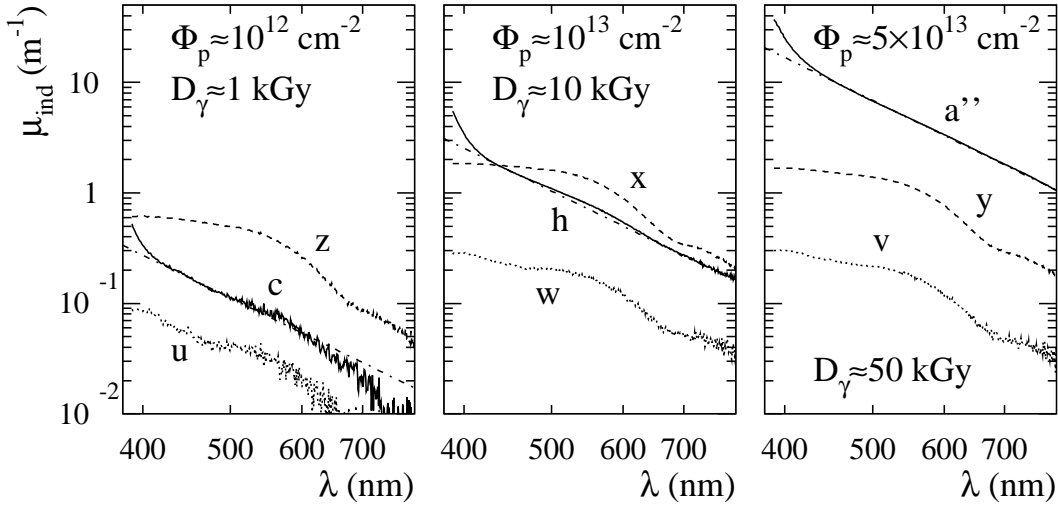


Figure 17: Plot of $\mu_{\text{IND}}(\lambda)$ against λ for proton and γ -damaged crystals exposed to different fluences and doses. The dot-dashed line shows λ^{-4} , fitted to the proton damage curve. The good agreement is an indication of Rayleigh scattering from small centres of severe damage.

- The damage corresponding to the two τ_i values is produced by proton and γ -irradiation in the same way and results in the same recovery-characteristics. Most likely this damage corresponds to the same color centres.
- The band-edge shift is unique to proton irradiation and corresponds to a different damage mechanism. This damage appears to be stable and cumulative, at least over the $\sum \Phi_p$ range explored.

A similar band-edge shift has been observed earlier in proton-irradiated BGO-crystals [26] while no such shift was created by γ -exposure. A later re-analysis of the data in [26] revealed that the proton induced damage is cumulative also in BGO [27].

The amplitudes A_1 and A_2 exhibit some dependence on proton fluence, which is not perfectly consistent with the above assumption. It is conceivable, however, that other defect centres, specific to protons, play some role and have time constants that could not be resolved from our two universal τ_i values and the constant term.

The assumption that the highly ionising fragments, produced by inelastic hadronic interactions, would be responsible for the observed specific proton damage implies that there might be very small regions of severe damage distributed within the crystal. Fig. 17 shows $\mu_{\text{IND}}(\lambda)$, plotted as a function of the wavelength. Above ~ 420 nm the dependency for heavily proton-damaged crystals goes like λ^{-4} , which is exactly what would result if the attenuation was entirely due to Rayleigh-scattering. In γ -damaged crystals no such linear dependence appears and only a structure due to absorption band formation is seen. The significant crystal-to-crystal variation of γ -damage is again evident. The $\mu_{\text{IND}}^{\text{std}}(420)$ values in Table 1 suggest that the proton-damaged crystals should rather be compared with the less damaged γ -irradiated crystals *u*, *w* and *v*. For proton damaged crystals, the λ^{-4} slope of Rayleigh-scattering is clearly superimposed on top of the absorption-band structure from pure ionisation damage. This provides firm evidence that the specific proton damage is of a very different nature than what can be caused by purely ionising radiation. At fluences of the order of 10^{12} cm^{-2} and below, the λ^{-4} slope starts to get submerged in the absorption band structure which means that at low fluences it would be difficult to distinguish the specific proton damage.

The $\mu_{\text{IND}}(\lambda)$ slope starts to deviate strongly from the λ^{-4} behaviour at wavelengths below 420 nm where the crystals become strongly absorptive. The Rayleigh scattering formalism is known to break down when the dimensions of the scattering centres become larger than $\sim 10\%$ of the wavelength. This means that the created defect centres must have dimensions $\ll 0.4 \mu\text{m}$.

The fact that proton damage seems to be connected to very small, highly damaged, regions strongly points in the direction that the origin is indeed in the heavily ionising fragments created in inelastic hadronic interactions. In this

case, the overall dose rate of the irradiations should not be significant, since the local instantaneous ionisation of the fragment is overwhelmingly large. Although the PS beam did not allow to lower the intensity in order to obtain firm experimental proof for this, all evidence supports the assumption that the proton damage will be cumulative irrespective of the dose rate.

8 Extrapolation to CMS at LHC

The high-precision ECAL will play a crucial role in the CMS experiment for the search of the Higgs boson and exploration of possible new physics beyond the Standard Model. The calorimeter comprises ~ 76000 PbWO_4 crystals, which provide hermetic coverage up to a pseudorapidity $\eta = 3.0$. In order to fully profit from the advantage of a homogeneous calorimeter, namely a very low stochastic term in the energy resolution, the constant term must be kept low as well. This can be achieved only by accurate calibration and permanent monitoring of the crystals. Radiation damage, not compensated by monitoring, would quickly degrade the calorimeter performance. Therefore, the LT of each crystal will be calibrated with a 440 nm laser. In addition $Z \rightarrow e^+e^-$ and $W \rightarrow e\nu$ events can be used for *in-situ* calibration. However, if the transparency of the crystals decreases, this will ultimately affect the photostatistics and thereby increase the stochastic term in an unrecoverable way.

The endcaps (EE) are the parts of the ECAL which are exposed to the harshest radiation environment. The area where high resolution is desirable extends to $|\eta| = 2.5$. The hadron spectrum incident on the EE varies with

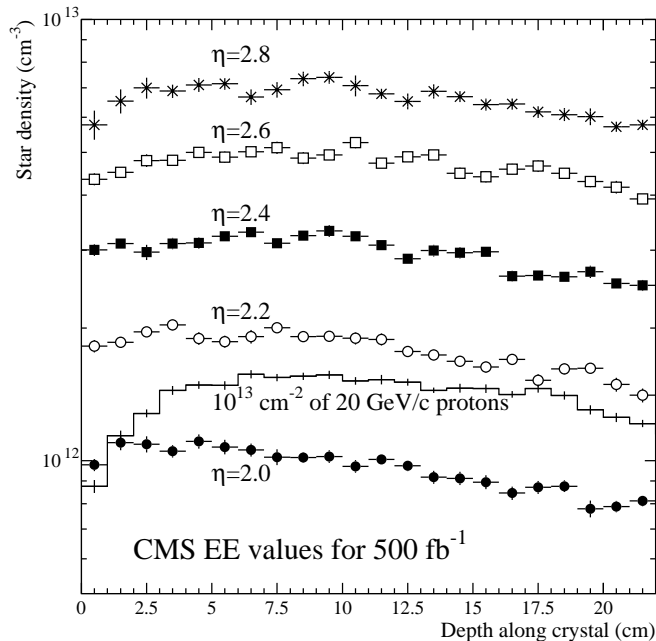


Figure 18: Star density at different η in the CMS endcap ECAL for 500 fb^{-1} integrated luminosity. The histogram shows the average star density in a single crystal irradiated with 10^{13} protons per cm^2 in the 20 GeV/c beam-line.

radius, but it is always broad and on average much less energetic than the 20 GeV/c proton beam used in our tests. In Fig. 18 we compare the simulated star densities at various η -values in the EE and along the centre of a crystal exposed to 10^{13} p/cm^2 at 20 GeV/c. In terms of pure star density, a fluence of $\Phi_p = 10^{13} \text{ cm}^{-2}$ of 20 GeV/c protons would correspond to the star density expected at $\eta \approx 2.2$ over 10 years LHC operation. However, the characteristics of stars change with energy. While in our beam test a majority of stars are generated by high-energy protons, in the EE they are predominantly due to pion and neutron interactions at energies rarely exceeding 1 GeV. At low energy typically a few nucleons are emitted and one heavy slow recoil is produced. With increasing energy, the multiplicity of secondary particles increases and the mean atomic mass of the heavy nuclear fragment decreases, while its energy increases slowly. Energies of fission fragments are fairly constant but the cross section is energy-dependent. These effects can be taken into account only by a detailed simulation of the hadron-nucleus events followed by transport of the fragments down to zero energy. However, prior to such a simulation, it has to

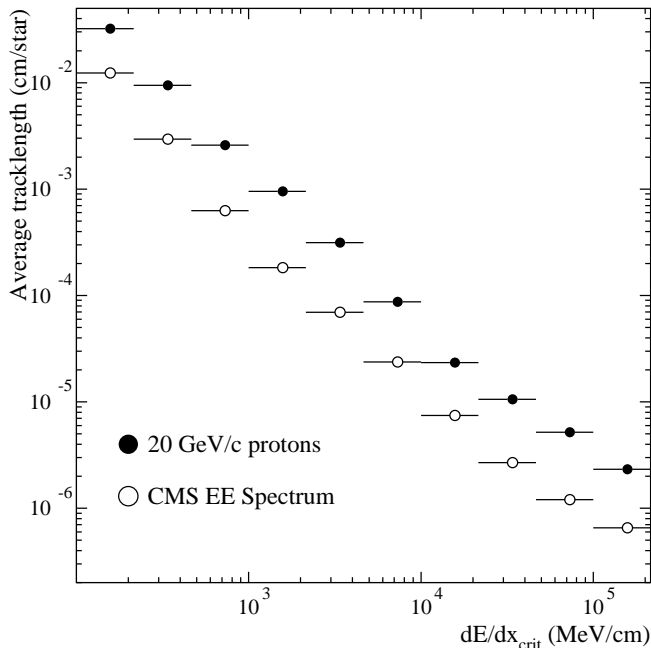


Figure 19: Average sum of tracklength per star with ionisation density above a given value of $(dE/dx)_{crit}$ for the beam test and for CMS endcap ECAL conditions.

be decided which is the physical process causing the damage.

We have argued that stars are likely to be at the origin of the specific proton damage and our experimental results – especially the consistency with Rayleigh scattering – seem to support this. However, our irradiation data do not tell us by what mechanism the stars cause the observed damage. In high-resistivity silicon the hadron damage is known to be due to the created impurities and, especially, lattice defects [28]. However, since the natural impurity concentrations in $PbWO_4$ are much higher, a similar damage mechanism cannot be assumed without a quantitative consideration. From Fig. 3 we deduce an average of 0.14 stars/cm³ per unit of flux. Thus, for $\Phi_p = 10^{13}$ cm⁻² we obtain an impurity concentration of about 3×10^{-11} per atom. This is far lower than the natural density of imperfections in the crystal, which is at the 10^{-6} level.

However, along their path, the recoils collide elastically with atoms of the lattice and kick these out from their position. Most of the displacements heal immediately, but some remain stable or metastable. Simulation methods of fragment transport have been developed for studies of Single Event Upsets in silicon based electronics chips [29]. Thereafter they have been successfully applied to bulk damage studies of silicon detectors [28]. Silicon, in contrast to $PbWO_4$, is a well known material from this point of view. Thus the adaption of the simulation to the crystals introduced several uncertainties. In particular, the displacement energy, about 20 eV in silicon, is not known for $PbWO_4$. While it is likely to be higher, it is unlikely to be much different from the silicon value. For our simulations we assume a value of 50 eV. The simulations proceed as described in [28, 29] and give on average 2700 displaced atoms per 20 GeV/c proton. Counting both the vacancies and the interstitials as defects, the number doubles. However, at least 90% of the vacancy-interstitial pairs will recombine immediately, so a reasonable assumption for the number of defects created per proton is <500 . This gives an upper limit of $\sim 10^{-8}$ for the defect concentration per lattice atom, which still remains about two orders of magnitude below the natural impurity levels.

A more plausible damage mechanism seems to be that the created nuclear fragments cause extremely high local ionisation densities along the short path which they cover in the crystal. It can be seen from Fig. 1 that a lead ion can reach a maximum dE/dx of 5×10^5 MeV/cm, which is 50000 times larger than for a minimum ionising particle. It is certain, however, that Pb fragments with 1 GeV kinetic energy will not be created by hadron-nucleus collisions. The most energetic fragments are due to high-energy induced fission of W and Pb and typically have energies of 100 MeV or just below. Zr and Fe, shown in Fig. 1, are good examples of possible fission products. Thus the maximum dE/dx of the fragments can be about 2×10^5 MeV/cm. If these very densely ionising fragments

are responsible for specific hadron damage, then the main question is what is the critical value $(dE/dx)_{\text{crit}}$ needed to create a stable damage centre. If such a value can be identified, then the amount of damage is quite likely to scale with the total tracklength of fragments exceeding $(dE/dx)_{\text{crit}}$. This tracklength is shown in Fig. 19 for $(dE/dx)_{\text{crit}}$ values above 100 MeV/cm. The tracklengths are normalized per star, which allows a direct comparison of the reactions induced by 20 GeV/c protons and those expected in the CMS EE, for which an average spectrum between $\eta=1.9-2.8$ has been used in the simulation. In order to be insensitive to the non-uniformity close to the crystal edges, the tracklengths were recorded only ± 5 mm around the centre line of the crystal, which corresponds to the region mapped in the LT measurements.

The difference in tracklength between the 20 GeV/c proton induced events and those created by the EE spectrum shows only a weak dependence on $(dE/dx)_{\text{crit}}$ and amounts on average to a factor of 4. At $(dE/dx)_{\text{crit}}$ below 1 GeV/cm, the tracklength is mostly due to slow protons. For these it should be noted that the simulations consider only protons produced by the stars. Especially in the CMS EE, but to some extent also in our beam test, protons produced elsewhere can enter the crystal and produce a highly ionising track upon stopping²⁾. For $(dE/dx)_{\text{crit}} > 1$ GeV, heavier fragments dominate because, as shown in Fig. 1, the dE/dx of a proton can never exceed 1.5 GeV/cm. It should be pointed out that the results of Fig. 19 are not sensitive to our assumption of 50 eV as the displacement threshold. That parameter affects only the total number of produced lattice defects, but not the highly ionising tracks.

With the provision that these simulations are based on an unproven assumption of the mechanism causing the specific hadron damage, Fig. 19 predicts that stars produced by our beam test are on average a factor of 4 more damaging than those expected in the EE. With 20 GeV/c protons the specific hadron damage becomes dominant at $\sum \Phi_p \approx 10^{13} \text{ cm}^{-2}$, when $\mu_{\text{IND}}(420) \approx 2 \text{ m}^{-1}$. Taking the factor of 4 into account but assuming that the damage is stable over time, this would correspond to roughly $\eta=2.6$ after an integrated LHC luminosity of 500 fb^{-1} . If this extrapolation is correct, the performance of the high-resolution region of the ECAL will not be compromised by hadron damage during the first 10 years of LHC operation.

9 Conclusions

We have performed an extensive irradiation campaign, aimed at verifying the possible existence of specific, hadron-induced damage in PbWO₄ crystals. Emphasis has been put on a careful analysis and detailed understanding of the irradiation conditions and a long follow-up of damage recovery.

The very intense radiation environment would have damaged any front-end electronics or other sensitive equipment, making a determination of damage on the crystal itself complicated if an *in situ* determination of LT had been attempted. To avoid such ambiguities we put our emphasis on a simple procedure aimed solely at the determination of long-term damage. Due to the high rates which we were forced to use in order to reach 10-year equivalent LHC fluences, any determination of short term damage would not have been relevant for LHC conditions, anyway.

Since no γ -irradiation data of recent CMS crystals existed at dose rates corresponding to those caused by the proton beam, we made comparative irradiations at an intense ⁶⁰Co facility.

Only at proton fluences well beyond 10^{12} cm^{-2} , i.e. doses much higher than 1 kGy, we start to observe clear differences in the LT-characteristics of crystals exposed to protons and those exposed to photons. The main differences are

1. The proton induced damage increases linearly with fluence while the γ -damage saturates after a few hours of exposure at 1 kGy/h.
2. No correlation is seen between the $\mu_{\text{IND}}^{\gamma\text{std}}(420)$, from the radiation hardness pre-characterisation with ⁶⁰Co photons, and the proton induced $\mu_{\text{IND}}(420)$. In the case of our γ -irradiated crystals this correlation is nearly perfect.
3. In proton-irradiated crystals, the band-edge shifts towards longer wavelengths and $\mu_{\text{IND}}(\lambda) \propto \lambda^{-4}$, while the band-edge remains stable in the γ -irradiated crystals and a clear absorption-band structure appears in $\mu_{\text{IND}}(\lambda)$.

²⁾ In the simulations for the EE, one crystal within a big matrix was considered, while for the beam test a single crystal in infinite void was simulated.

4. After $\sum \Phi_p = 5.4 \times 10^{13} \text{ cm}^{-2}$, i.e. $\sim 100 \text{ kGy}$, we observe $\mu_{\text{IND}}(420) \approx 15 \text{ m}^{-1}$ and a linear rise with fluence. For a crystal with similar radiation-hardness characteristics, we observe after a γ -dose of $\sim 50 \text{ kGy}$ only $\mu_{\text{IND}}(420) = 0.3 \text{ m}^{-1}$ and no indication of further increase towards higher doses.

It was not possible to raise the γ -intensity beyond 1 kGy/h , in order to obtain a comparison with our highest proton beam intensities. It is usually claimed that the saturation level of γ -damage increases with dose rate. For protons, however, we observe no difference between rates of $10^{12} \text{ cm}^{-2}\text{h}^{-1}$ and $10^{13} \text{ cm}^{-2}\text{h}^{-1}$.

A thorough exploration of fitting various functions to the recovery data showed, that Eq. 3 is suitable to fit all data accumulated so far. In particular we discovered that the quality of the fits does not suffer, if the time constants, τ_i , are universal with values of 17.2 days and 650 days. Only the absolute amount of damage is very different for the two radiation types, which is reflected in a different dose dependence for the fitted amplitudes A_i , as shown in Fig. 13.

Our results provide strong evidence that proton exposure of PbWO_4 crystals causes damage that cannot be reproduced with γ -irradiation. This damage seems to be independent of rate and increases linearly with accumulated fluence. We strongly emphasise that the difference we observe starts to manifest itself only at proton fluences well beyond 10^{12} cm^{-2} . Below this fluence the “normal” γ -like damage, due to minimum ionising tracks, is dominating to such an extent that it is probably impossible to experimentally see any difference between protons and photons.

The observation, that $\mu_{\text{IND}}(\lambda)$ of proton damaged crystals is consistent with Rayleigh scattering from objects much smaller than $0.4 \mu\text{m}$, supports our assumption that the specific proton damage is due to the very dense local ionisation of fragments created in inelastic nuclear collisions. In this case it is likely that the 20 GeV/c proton beam used in our tests is somewhat too pessimistic with respect to the hadron spectrum expected in the CMS ECAL. Our simulations indicate that the damage ratio between 20 GeV/c protons and the CMS ECAL hadron spectrum, per unit star density, might be about a factor of 4. But this remains to be verified by further irradiations with low-energy pions, which provide a better representation of the ECAL conditions.

A Induced radioactivity

The creation of nuclear fragments during hadron irradiation causes the crystals to become radioactive. Since PbWO_4 includes the heavy elements W and Pb, the 20 GeV/c proton beam is able to produce a huge number of different nuclides. Most of these are either stable or short-lived, but a fraction of them have long half-life and are responsible for the remnant radioactivity of the irradiated crystals. According to simulations, there are about 1800 different nuclide species with an activity above 1 Bq/cm^3 at the end of an exposure to 10^{13} p/cm^2 . Even after 50 days of cooling, 150 nuclides remain above this activity threshold.

The predictive simulation of crystal radioactivation proceeded in three steps. First, during the full FLUKA simulation described before, all residual nuclides produced in the crystal were recorded. This stage relies on the accuracy of the FLUKA models to describe the hadron-nucleus interaction in full detail. Earlier dedicated work has shown, that an accuracy better than a factor of 2 can be expected for heavy materials [30, 31]. In a second stage the evolution over time of the produced nuclide inventory was calculated with the DeTra code [32]. This calculation is analytical and thus exact within the limits of accuracy given by the available nuclear data files. DeTra produces a table of all nuclide activities as a function of cooling time. For the final phase of the simulation these activities were converted into an emitted γ -spectrum which was then used to calculate \dot{D}_{ind} at our measurement point by integrating over the entire crystal and weighting with the simulated star density within the crystal. The integration was performed via a detailed photon transport with FLUKA.

Figure 20 compares simulated \dot{D}_{ind} and all our measurements. For this purpose all measurements have been rescaled to $\sum \Phi_p = 10^{13} \text{ cm}^{-2}$, using the total proton fluence, as determined from activation of aluminium foils. The two curves in Fig. 20, corresponding to different beam intensities but the same integral $\sum \Phi_p$, show that by the time our measurements could begin only the value of $\sum \Phi_p$ matters, not the rate. Thus a rescaling by $\sum \Phi_p$ is justified for our comparison.

In the small insert of Fig. 20 the doses from individual crystals are compared with the calculated \dot{D}_{ind} . We observe a systematic underestimate in the simulation. On average the deviation amounts to 29% and even at worst the disagreement remains below a factor of 2, which still can be considered a very good agreement for such a prediction. We also have to recall two uncertainties in the measured values with respect to the simulation, namely the unknown efficiency of the Automess 6150AD6 above 1.3 MeV , which we probably underestimate, and a slight uncertainty in the size and position of the sensitive element within the device.

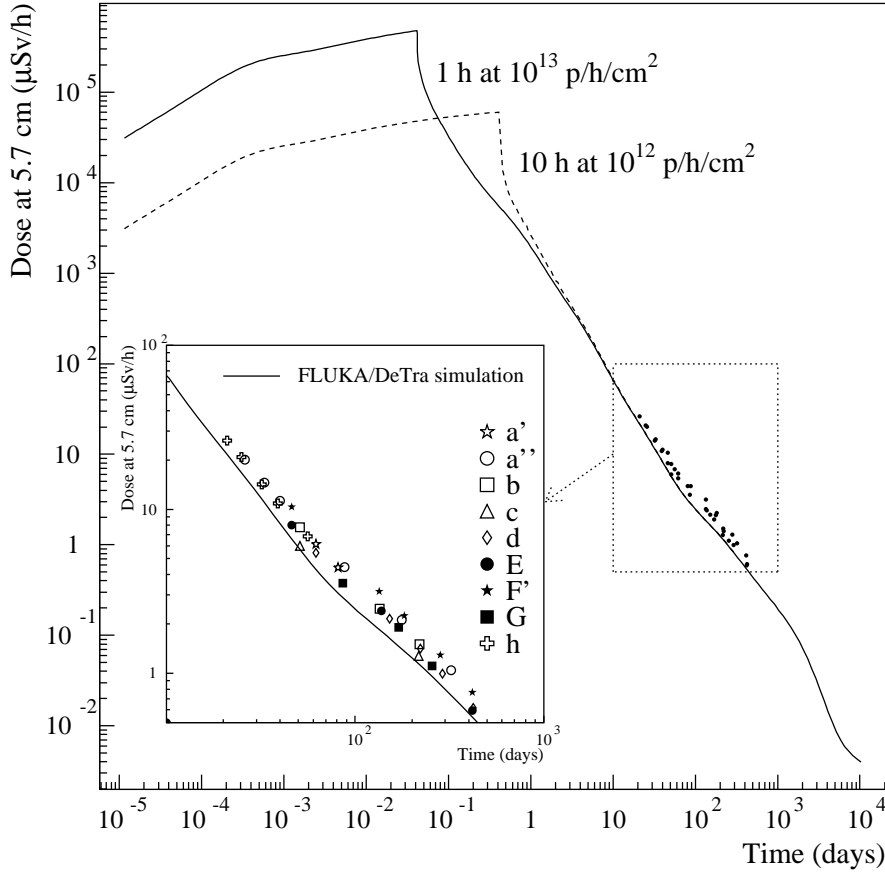


Figure 20: Comparison of simulated and measured radioactivity as a function of cooling time. All data have been renormalised to $\sum \Phi_p = 10^{13} \text{ cm}^{-2} \text{ h}^{-1}$ using the fluence information from Al foils, as given in the $\sum \Phi_p$ column of Table 3.

	Front	Middle	Rear
Measured	7.67	10.4	8.64
Calculated	5.09	6.58	5.48
$1.58 \times \text{Calc}/\text{Meas}$	1.05	1.00	1.00

Table 5: Measured and calculated \dot{D}_{ind} ($\mu\text{Sv/h}$) close to the front, in the middle and close to the rear of crystal a'' (see Table 3). The values correspond to 177 days cooling after the last irradiation.

We used the \dot{D}_{ind} measurements also to cross-check the longitudinal star density simulations shown in Fig. 3. For this purpose we measured \dot{D}_{ind} , in addition to the middle, also close to the front and back of crystal a'' , which had been exposed to $\sum \Phi_p = 5.4 \times 10^{13} \text{ cm}^{-2}$. The results are given in Table 5. Correcting for the systematic underestimate of the simulations in the case of a'' , the relative front–middle–back ratios are very well reproduced³⁾. This good agreement increased our confidence that the simulations, summarised in Figs. 3 and 4, describe well the conditions within the crystal.

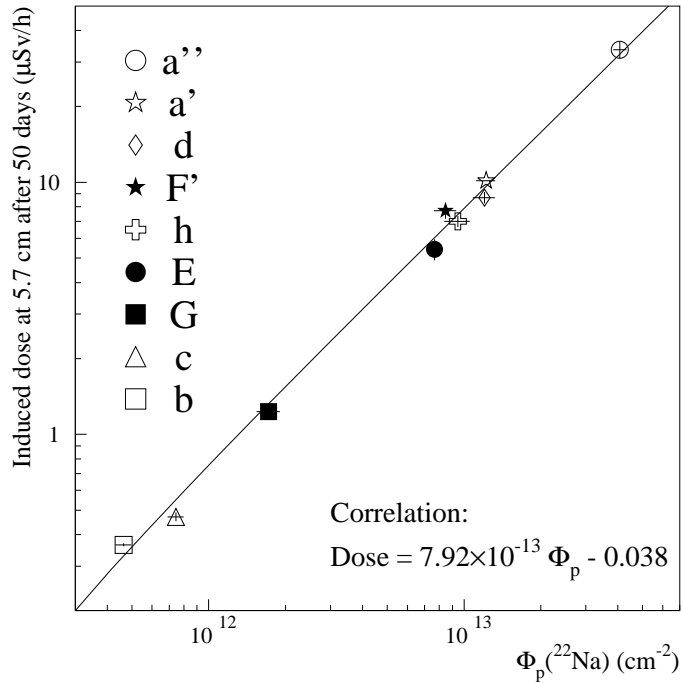


Figure 21: Correlation of measured \dot{D}_{ind} of the crystals and Φ_p as determined from ^{22}Na activity in the Al foils.

B Technical aspects of Φ_p determination

The most reliable standard way to determine the fluence of the incident proton beam (Φ_p) is by means of aluminium activation measuring the production of ^{24}Na . This is the isotope for which cross sections are known most reliably. However, the cross section $\text{Al}(n,\alpha)^{24}\text{Na}$ above ~ 6 MeV is much larger⁴⁾ than the $\text{Al}(p,X)^{24}\text{Na}$ cross section at 20 GeV (8.7 mb). Since the crystal produces a large flux of neutrons above this threshold energy, ^{24}Na is not a useful isotope to monitor Φ_p , on top of the fact that its 15 h half-life makes it impractical for our purpose. A more suitable isotope is ^{22}Na . Due to its long half-life it integrates the fluence, and is insensitive to short-term beam fluctuations.

The cross section for $\text{Al}(p,X)^{22}\text{Na}$ at ~ 20 GeV is not known as accurately as for $\text{Al}(p,X)^{24}\text{Na}$. Data in [34] exhibit a significant spread but allow us to estimate 11.2 ± 1.6 mb. The ratio $^{24}\text{Na}/^{22}\text{Na}$ in a foil, irradiated in the absence of a crystal, gave 10.4 mb. Since this is based on the much better known production cross section of ^{24}Na , we use 10.4 mb for the fluence analysis. However, we have to point out that even without a crystal, backscattered radiation in IRRAD1 increases the production of ^{24}Na more than of ^{22}Na . Thus the 10.4 mb is likely to represent a lower bound. Consequently, Φ_p is likely to be rather over- than underestimated.

While certainly smaller than for $\text{Al}(n,\alpha)^{24}\text{Na}$, the cross sections for $\text{Al}(n,X)^{22}\text{Na}$ are not known well enough to allow for an accurate analysis of the neutron contribution. With our best knowledge of the cross sections we obtain from the FLUKA simulation a 11% contribution to the ^{22}Na activity from non-beam particles. This we propagate into our estimate of the incident proton fluence.

The aluminium foils were cut to a size of $24 \times 24 \text{ mm}^2$, which roughly corresponds to the average crystal dimensions. Thus the foils were averaging the whole fluence incident on the crystal. In a single crystal, however, protons close to an edge contribute on average less star density, thus damage and activation, because a larger fraction of the hadronic cascade escapes, when compared to centrally impinging ones. In fact, the leakage of the cascade causes that the radiation intensity drops towards the edges even with a uniform beam, for which the star density in the centre is about 17% higher than the average over the whole crystal. However, would the crystal be surrounded by

³⁾ The values in front and back are particularly sensitive to the exact longitudinal position and the assumed size of the sensitive element in the 6150AD6.

⁴⁾ The $\text{Al}(n,\alpha)^{24}\text{Na}$ cross section exceeds 100 mb between 10–30 MeV and then decreases towards higher energies [33].

other crystals, also covered by the beam, then these would compensate for the leakage and the profile would be flat and the total star density higher. Thus the relation between Φ_p , determined with the aluminium foil, and the star density depends – in addition to the beam characteristics – also on the size and surroundings of the crystal.

The activation of the crystal by inelastic nuclear interactions is roughly proportional to the star density inside the crystal. Unfortunately, this does not provide an absolute determination of Φ_p , because star density and \dot{D}_{ind} can be related to each other only through simulations, which introduce too large an uncertainty, as discussed in detail in appendix A. However, since for all our irradiations the conditions within the crystals are the same, the effects of simulations cancel out if we consider only the relative differences between irradiations. Thus we expect a near to perfect correlation between \dot{D}_{ind} and the ^{22}Na activity of the aluminium foils. The only deviations could arise from significant non-uniformities of the beam spot or from a severe misalignment of the crystal during irradiation and, to a lesser extent, from the decay corrections, for which recourse to simulation is unavoidable. This correlation between Φ_p and \dot{D}_{ind} , shown in Fig. 21, provided a very valuable cross-check of our fluence measurements. The \dot{D}_{ind} measurements were taken at different times, but all values have been corrected to 50 days after irradiation using the simulated decay of radioactivity in the crystals. As expected, the correlation is almost perfect, indicating that the activation foils give reliable and consistent fluence values. There are no signs of severe anomalies in any individual irradiation.

Due to a faulty magnet in the PS, the early irradiations took place with a 20 GeV/c proton beam while later exposures (crystals *a''* and *h*) were performed at 24 GeV/c. The energy dependence of the $\text{Al}(p,X)\text{Na}^{22}$ cross section is negligible in this regime. However, as shown in Fig. 3, the 20% increase in proton momentum leads to more intense showering and thus to a higher radiation field within the crystal. The effect is very similar for all hadronic radiation quantities plotted in Fig. 3 but we use the 8.6% increase in star density, averaged over the crystal length. The LT measurements also average along the whole crystal and thus justify a simple correction by simply rescaling Φ_p , as determined from the aluminium foils, by a factor of 1.086 for the two crystals irradiated with 24 GeV/c protons. In the case of ionising dose the effect is larger because the electromagnetic cascade is much better contained even in a single crystal.

C Influence of beam non-uniformities

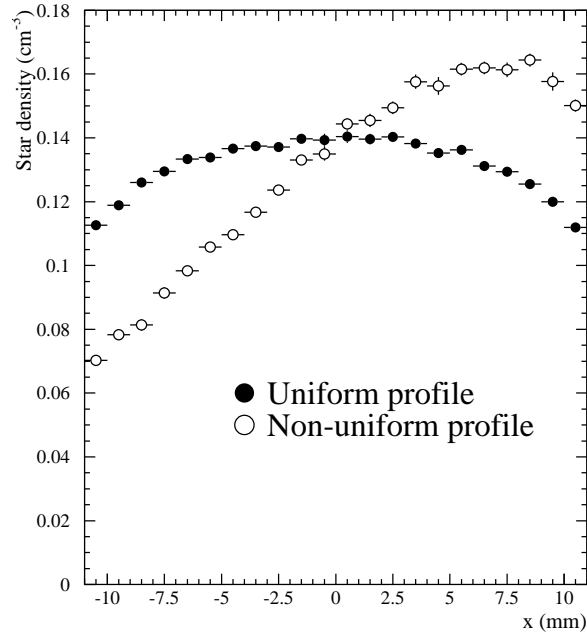


Figure 22: Transverse star-density profiles across a crystal for a perfectly uniform beam and for a beam with 5 times lower intensity at $x=-12$ mm than at $x=12$ mm.

In order to study the effect of non-uniformities of the beam, we assumed that the beam intensity drops linearly

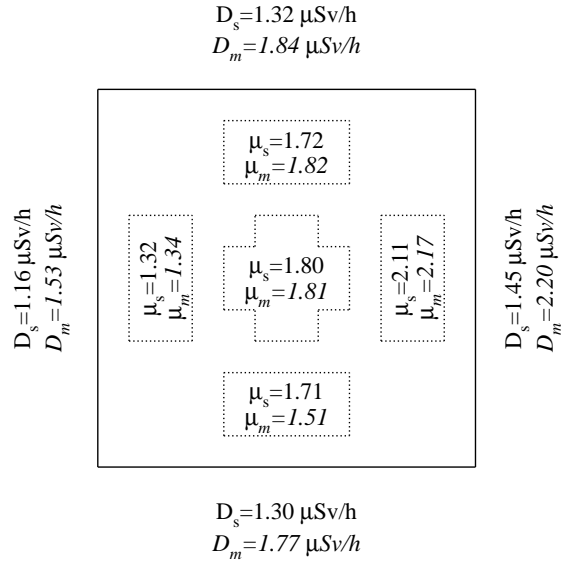


Figure 23: Effect of beam non-uniformity in case of crystal *E*. Compared are the \dot{D}_{ind} at 4.5 cm distance from each long side and the $\mu_{\text{IND}}(420)$ -values in the centre and close to each side. The measured values are labeled with 'm' and the simulated ones with 's'.

from one side of the crystal to the other⁵⁾. Crystal *E* was identified as having received the most non-uniform exposure. We adjusted the slope such that the \dot{D}_{ind} values measured on *E* were roughly reproduced and ended up with a factor of 5 intensity difference across the crystal front face. A full FLUKA simulation was done with such a severe non-uniformity. Fig. 22 compares the lateral profiles of star density obtained from this simulation and the normal uniform one. Although a larger fraction of beam hits close to the edge, the total number of stars differs only by a few percent. Due to cascading, the variation in star density is much smaller than the factor of 5 used as incident beam intensity. We also observe that in the centre of the crystal the effects of non-uniformity are at a minimum, which suggests that, provided the crystal alignment is the same in all LT measurements, even for the most severe beam non-uniformity encountered the influence on the results remains negligible in comparison to other uncertainties.

The factor of 5 beam intensity difference used in the simulations of a non-uniform beam, as described before, was adjusted so that the relative⁶⁾ variation of \dot{D}_{ind} observed on the most non-uniform crystal, *E*, was reproduced when the simulated data were used to calculate \dot{D}_{ind} on each side.

The same simulated data were also used to integrate the star density along the light paths of the LT measurements. Assuming that stars cause the damage, the fit of Fig. 15 allows to translate these star densities into $\mu_{\text{IND}}(420)$ values, which can be compared with the measured values on absolute scale.

Figure 23 shows such comparisons for \dot{D}_{ind} and $\mu_{\text{IND}}(420)$ in the case of crystal *E*. The systematic underestimate of \dot{D}_{ind} is consistent with Fig. 20, where the simulated \dot{D}_{ind} -values for crystal *E* are also slightly lower than the measurements. However, it must be emphasised that for such a simulation an agreement better than a factor of two, is remarkable.

The simulated $\mu_{\text{IND}}(420)$ values are in perfect agreement with measurements, except for a slight up-down asymmetry. This is most probably related to a beam non-uniformity in the vertical direction, while the simulated beam intensity was varied only horizontally.

⁵⁾ A determination of the beam profile using OSL (Optically Stimulated Luminescence) films showed that the real non-uniformities are not linear but exhibit a bump-like maximum on one side.

⁶⁾ The absolute value of $\sum \Phi_p$ is always derived from the aluminium foils.

In relative terms, the non-uniformities in both $\mu_{\text{IND}}(420)$ and \dot{D}_{ind} are very well reproduced by just considering the spatial variation of star density within the crystal.

Acknowledgements

The proton irradiations, performed at CERN, were made possible only by the efforts of R. Steerenberg, who provided us with the required PS beam conditions. The help of M. Glaser and F. Ravotti in operating the irradiation and dosimetry facilities is gratefully acknowledged. The support and practical help of S. Baccaro and A. Cecilia during the γ -irradiations at ENEA-Casaccia was essential and is gratefully acknowledged, as is the contribution of E. Auffray who provided us with the crystals after having characterised their γ -radiation hardness at the Geneva Hospital.

References

- [1] The CMS Collaboration, *The ECAL Technical Design Report*, CERN/LHCC 97-33 (1997).
- [2] The ALICE Collaboration, *Technical Design Report of the Photon Spectrometer (PHOS)*, CERN/LHCC 99-4 (1999).
- [3] The BTeV Collaboration, *Experiment to Measure Mixing, CP Violation and Rare Decays in Charm and Beauty Particle Decays at the Fermilab Collider – BTeV*, Fermilab-P819, May, 2000.
- [4] Proc. SCINT97, Int. Conf. on Inorganic Scintillators and their Applications, Shanghai, China, 1997, eds Z. W. Yin *et al.*
- [5] X. Qu, Z. Zhu and R.-y. Zhu, IEEE, Trans. Nucl. Sci. NS-47 (2000) 1741.
- [6] A. A. Annenkov, M. V. Korzhik and P. Lecoq, Nucl. Instr. and Meth. A490 (2002) 30.
- [7] P. Lecoq, *Ten years of lead tungstate development*, Nucl. Instr. and Meth. (2004), in press.
- [8] H. F. Chen, *et al*, Nucl. Instr. and Meth. A414 (1998) 149.
- [9] H. Hofer, P. Lecomte and F. Nessi-Tedaldi, Nucl. Instr. and Meth. A433 (1999) 630.
- [10] R. Chipaux and O. Toson, CERN CMS TN/95-126 and Proc. SCINT95, Int. Conf. on Inorganic Scintillators and their Applications, p 274, Delft, The Netherlands, 1995, eds P. Dorenbos and C. W. E. vanEick.
- [11] E. Auffray *et al*, CERN CMS NOTE-1998/069 (1998).
- [12] V. A. Batarin *et al.*, Nucl. Instr. and Meth. A530 (2004) 286.
- [13] M. Huhtinen, CERN CMS NOTE-1998/055 (1998).
- [14] T. Enqvist *et al*, Nucl. Phys. A686 (2001) 481.
- [15] E. Auffray, *et al*, CERN CMS NOTE 1998/038 (1998).
- [16] E. Auffray, private communication.
- [17] M. Glaser *et al*, Nucl. Instr. and Meth. A426 (1999) 72.
- [18] *Gebrauchsanweisung für den Dosisleistungsmesser 6150AD6*, Automation und Messtechnik AG, Ladenburg, Germany, 2001.
- [19] P. A. Aarnio *et al*, CERN TIS-RP/168 (1986) and CERN TIS-RP/190 (1987) .
A. Fassò *et al*, Proc IV Int. Conf. on Calorimetry in High Energy Physics, La Biodola, eds. A. Menzione and A. Scribano, World Scientific, p. 493 (1993).
P. Aarnio and M. Huhtinen, Proc MC93, Int. Conf. on Monte Carlo Simulation in High Energy and Nuclear Physics, p 1, eds. P. Dragowitsch, S. Linn and M. Burbank, World Scientific (1994).
A. Fassò *et al*, Specialists' Meeting on Shielding Aspects of Accelerators, Targets and Irradiation Facilities. Arlington, Texas, April 28-29, 1994. NEA/OECD doc. p. 287 (1995).

- [20] Q. Deng, Z. Yin and R-y. Zhu, Nucl. Instr. and Meth. A438 (1999) 415.
- [21] J. Ranft and K. Goebel, CERN Health Physics Group, Internal Report, HP-70-92 (1970).
- [22] M. Huhtinen and L. Nicolas, CERN CMS NOTE-2002/019 (2002).
- [23] S. Baccaro, A. Festinesi and B. Borgia, CERN CMS TN-1995/192 (1995)
- [24] H. Vincke, private communication.
- [25] R. Y. Zhu, *Precision CMS PWO Crystal ECAL*, presentation at IEEE NSS/MIC03 conference, Portland, October 20, 2003.
- [26] M. Kobayashi *et al*, Nucl. Instr. and Meth. A206 (1983) 107.
- [27] F. Nessi-Tedaldi, *Crystals for high-energy calorimetry in extreme environments*, presentation at the DPF2004 meeting, Riverside, USA, August 26–31, 2004, preprint ETHZ-IPP-PR-2004-02 (2004).
- [28] M. Huhtinen, Nucl. Instr. and Meth. A491 (2002) 194.
- [29] M. Huhtinen and F. Faccio, Nucl. Instr. and Meth. A450 (2000) 155.
- [30] P. Aarnio, T. Hakulinen and M. Huhtinen, J. Radioanal. Nucl. Chem. Vol 248, No 2 (2001) 385.
- [31] P. Aarnio, J. Ala-Heikkilä, T. Hakulinen and M. Huhtinen, “High-Energy Proton Irradiation and Induced Radioactivity Analysis of Some Construction Materials for the CERN LHC”, J. Radioanal. Nucl. Chem. Vol 264 (2005) in press.
- [32] P. A. Aarnio, CERN CMS NOTE-1998/086 (1998).
- [33] M. Huhtinen, CERN CMS IN-2001/012 (2001).
- [34] A. S. Iljinov *et al*, *Radionuklidproduktion bei mittleren Energien*, Landolt-Börnstein, Neue Serie, Band 13a, Springer 1991.